Origin and geochemical evolution of the Madeira-Tore Rise (eastern North Atlantic)

Jörg Geldmacher,[1] Kaj Hoernle,[1] Andreas Klügel,[2] Paul v. d. Bogaard,[1] Frank Wombacher,[1,3] and Björn Berning[4,5]

[1]   The Madeira-Tore Rise, located ∼700 km off the NW African coast, forms a prominent ridge in the east Atlantic. The age and origin of the rise are controversial. This study presents major and trace element, Sr, Nd, Pb, Hf isotope and $^{40}Ar/^{39}Ar$ age determinations from volcanic rocks dredged from different sites along the rise. In addition, isotopic compositions of rock samples from Great Meteor Seamount in the central Atlantic are presented. The new radiometric and paleontologically constrained ages identify two major episodes of volcanism: The first is the base of the rise (circa 80 to >95 Ma) and the second is seamounts on the rise (0.5–16 Ma). It is proposed that interaction of the Canary hot spot with the Mid-Atlantic spreading center formed the deep basement of the Madeira-Tore Rise and the J-Anomaly Ridge west of the Atlantic spreading center in the Mid-Cretaceous. Age and geochemical data and plate tectonic reconstructions suggest, however, that the recovered Late Cretaceous volcanic rocks represent late stage volcanism from the time when the Madeira-Tore Rise was still close to the Canary hot spot. Long after moving away from the influence of the Canary hot spot, the Madeira-Tore Rise was overprinted by late Cenozoic volcanism. Miocene to Pleistocene volcanism at the northern end of the rise can be best explained by decompression mantle melting beneath extensional sectors of the Azores-Gibraltar Fracture Zone (African-Eurasian plate boundary). The geochemical compositions of these volcanic rocks suggest that the magmas were variably contaminated by enriched material within or derived by melting of enriched material underplated at the base of the lithosphere, possibly originating from the Cretaceous Canary plume. Alternatively, these late Cenozoic volcanic rocks may have derived from decompression melting of enriched pyroxenitic/eclogitic material in the upper mantle. Isotopically more depleted Pliocene to Pleistocene volcanism at the southern end of the Madeira-Tore Rise may be related to the nearby Madeira hot spot.

1.   Introduction

[2]   The ∼1000 km long Madeira-Tore Rise (MTR) is a complex, NE trending submarine ridge in the central east Atlantic that rises from >4000 m water depths to as shallow as 150 m below sea level. The MTR is bounded by abyssal plains to the west and south and by a number of large isolated seamounts on its eastern side (Gorringe Bank, Hirondel, Ampère/Coral Patch, Unicorn, Seine) and the Madeira Islands to the southeast (Figure 1). The northern termination of the MTR is formed by the active Azores Gibraltar Fracture Zone system ("Gloria Fault") that is part of the Africa-Eurasia plate boundary [e.g., *Jiménez-Munt et al.*, 2001]. The exact location of this boundary north and to the east of the MTR is not precisely known. On the basis of morphology, the main fault zone seems to cut the northern part of the MTR near Josephine Seamount and continues along Hirondel Seamount and Gorringe Bank to the Iberian continental rise. A 200 km wide zone of diffuse seismicity, however, suggests that interaction between the African and Eurasian plates in this region is occurring over a broad zone rather than along a distinct boundary [*Peirce and Barton*, 1991]. South of the Azores-Gibraltar Fracture Zone, the MTR forms a broad plateau with several large seamounts on its eastern flank (e.g., Josephine, Erik, Lion, and Dragon seamounts).

[3]   The age and origin of the MTR is a long-standing question. Early expeditions recovered volcanic rocks from the top of Josephine Seamount, the highest structure on the MTR located near its northern end [e.g., *Eckhard et al.*, 1977]. Models proposed for the formation of the MTR

¹Leibniz Institute of Marine Sciences, IFM-GEOMAR, Kiel, Germany.
²Department of Geosciences, Universität Bremen, Bremen, Germany.
³Now at FR Geochemistry, Freie Universität Berlin, Berlin, Germany.
⁴Institute of Geology/Paleontology, Universität Hamburg, Hamburg, Germany.
⁵Now at Institute of Geology and Paleontology, Universität Graz, Graz, Austria.
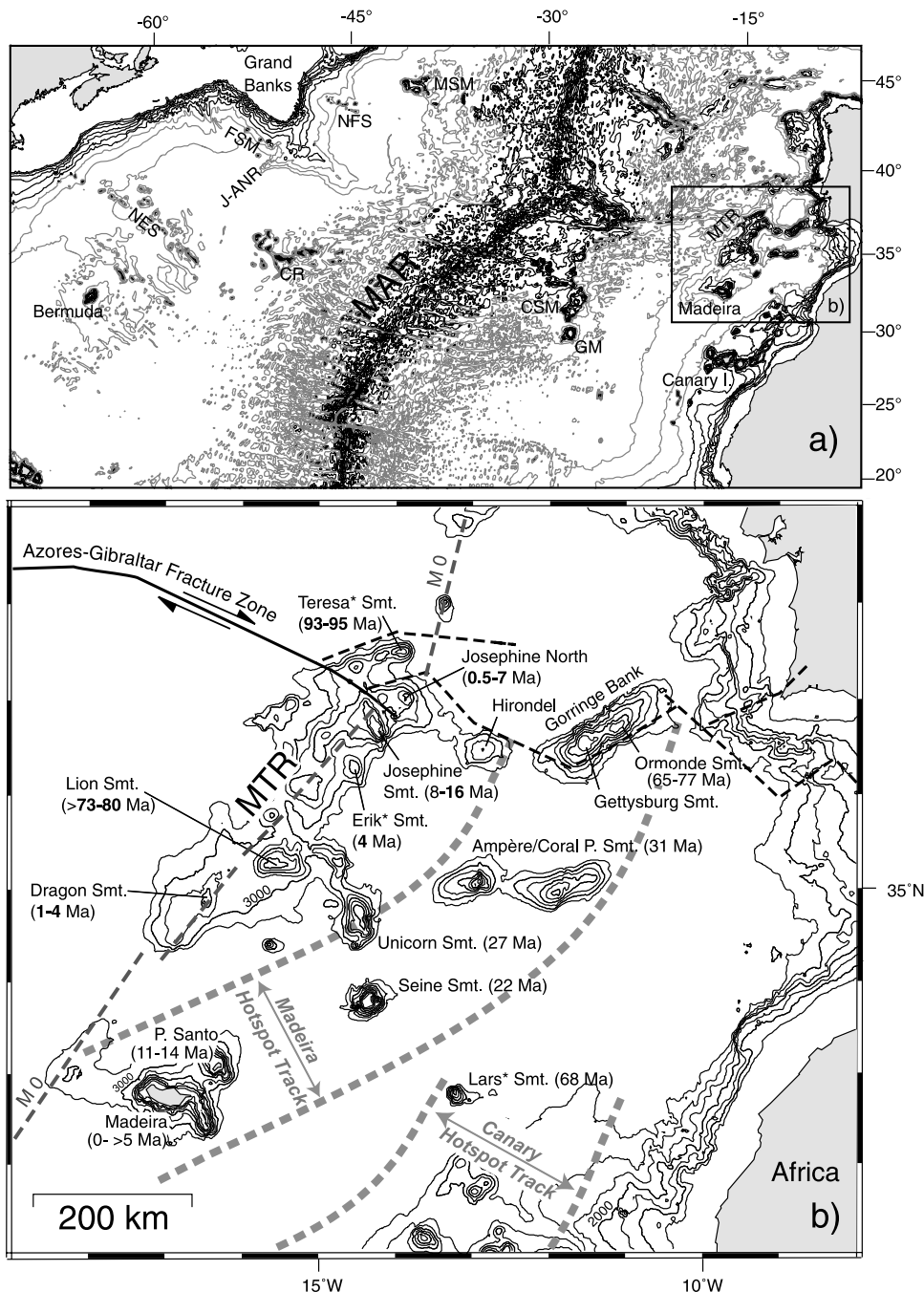
Figure 1. (a) Bathymetric map of the central Atlantic. MAR, Mid-Atlantic Ridge; NFS, Newfoundland seamounts; MSM, Milne seamounts; FSM, Fogo seamounts; J-ANR, J-Anomaly Ridge; NES, New England seamounts; CR, Corner Rise; CSM, Cruiser seamounts; GM, Great Meteor Seamount; MTR, Madeira-Tore Rise. Source is GEBCO [*Intergovernmental Oceanographic Commission et al.*, 1994], 500 m depth intervals, to highlight prominent structures depths contours below 3500 m are shown in gray). (b) Bathymetric map of the Madeira-Tore Rise (MTR) and neighboring seamounts of the Madeira and Canary hot spot track (framed with heavy gray dashed lines) from TOPEX [*Smith and Sandwell*, 1997]. Only depth contours above 3500 m are shown for clarity. Ages determined in this study for individual MTR seamounts are shown in bold. For all other age data, see *Geldmacher et al.* [2005] for reference. Asterisks mark working names for unnamed seamounts. Location of the Azores-Gibraltar Fracture Zone system is compiled after *Jiménez-Munt and Negredo* [2003] and *Kaz'min et al.* [1990]. M 0 magnetic anomaly is after *Roeser et al.* [2002] and *Klitgord and Schouten* [1986].

Table 1. Sampling Sites

Dredge Site	Area	Location	Coordinates
		Madeira-Tore Rise	
403	deep northern flank of the MTR	Teresa Seamount[a] (3200–2846 m)	37°33.80 N, 13°49.50 W
399	Josephine North area	Pico Pia[a] (1464–1231 m)	36°58.90 N, 13°48.80 W
406	Josephine North area	Toblerone Ridge[a] (1930–1592 m)	36°55.31 N, 14°02.83 W
407	Josephine North area	Pico Julia[a] (2200–1960 m)	36°41.70 N, 14°01.42 W
101[b]	Josephine Seamount	top (170–195 m)	36°63.6 N, 14°23.6 W
123[b]	Josephine Seamount	top (231–210 m)	36°67.5 N, 14°25.3 W
129[b]	Josephine Seamount	upper flank (740–655 m)	
133[b]	Josephine Seamount	upper flank (430–260 m)	36°66.6 N, 14°29.5 W
408	Josephine Seamount	eastern slope (3600–3053 m)	36°30.54 N, 14°10.21 W
409	Josephine Seamount	western slope (1303–1200 m)	36°35.03 N, 14°16.17 W
410	Josephine Seamount	southern slope (2436–2161 m)	36°30.46 N, 14°12.48 W
412	Erik Seamount[a]	southeastern flank (2198–1839 m)	36°10.23 N, 14°29.59 W
421	Lion Seamount	southern flank (2100–1809 m)	35°10.10 N, 15°29.28 W
429	Dragon Seamount	northern flank (2456–2173 m)	35°04.59 N, 16°21.37 W
431	Dragon Seamount	summit (1675–1286 m)	34°54.12 N, 16°28.26 W
		Seamounts off the MTR (Along the AGFZ)[c]	
391	Ormonde Seamount (Gorringe Bank)	northern flank (1250–1202 m)	36°44.67 N, 11°15.82 W
		Great Meteor Seamount	
173[b]	Great Meteor Seamount	upper flank (960–600 m)	29°70.3 N, 28°34.2 W
178[b]	Great Meteor Seamount	flank (1000–600 m)	29°96.5 N, 28°26.2 W

[a]Working names given to unnamed seamounts.
[b]Dredge hauls from *Meteor* expedition M9 [*Closs et al.*, 1968].
[c]Azores Gibraltar Fracture Zone.

include an origin as (1) a Cretaceous aseismic ridge formed at the Mid-Atlantic Ridge [*Tucholke and Ludwig*, 1982; *Peirce and Barton*, 1991], (2) an uplifted thrust belt of an active east dipping subduction zone [*Royden*, 1993], (3) a hot spot track [e.g., *Morgan*, 1983], and (4) diffuse volcanism resulting from upper mantle convection currents and subsequent decompression melting at the edge of the African continent [e.g., *King and Anderson*, 1998]. The lack of additional age and geochemical data from the MTR has prevented any further investigation of these hypotheses.

[4] Isolated seamounts to the southeast of the MTR (Ampère, Coral Patch, Unicorn and Seine seamounts) and the Madeira Archipelago have been the focus of several recent studies. These volcanic rocks are characterized by ocean island basalt (OIB) major and trace element and isotopic compositions [*Mata et al.*, 1998; *Geldmacher and Hoernle*, 2000; *Geldmacher et al.*, 2005]. The following age progression from SW to NE is observed: Madeira/Desertas volcanic complex (0–6 Ma), Porto Santo Island (11–14 Ma), Seine Seamount (22 Ma), Unicorn Seamount (27 Ma), Ampere Seamount (31 Ma), and the volcanic summit of Ormonde Seamount (65–77 Ma) [e.g., *Geldmacher et al.*, 2000, 2005; *Féraud et al.*, 1982, 1986; *Schärer et al.*, 2000]. The OIB-type geochemistry and age progression are consistent with these volcanoes forming a 700 km long hot spot track. It remains unclear, however, if and to what extent the MTR is related to the Madeira hot spot. As is seen in Figure 1b, the elongation of the rise does not point to Madeira but rather to the west of it following the trend of the M-0 magnetic anomaly.

[5] Several seamounts and structures on the MTR were mapped and sampled during the R/V *Meteor* cruise M51/1 (12 September to 15 October 2001 [*Hoernle and Scientific Party*, 2003]). Coordinates and water depths of sampling sites are given in Table 1. This study presents $^{40}Ar/^{39}Ar$ age determinations, and major and trace element and isotopic (Sr, Nd, Pb, Hf) data of the recovered rock samples in order

to determine the origin of the MTR and to improve our understanding of the early history of the eastern North Atlantic ocean basin.

2. Geological Overview and Sample Description

2.1. Northern Madeira-Tore Rise

[6] The Azores-Gibraltar fault system runs through the northern end of the MTR resulting in a complex bathymetry. The region is dominated by Josephine Seamount, peaking at depths of ~130 m below sea level (bsl). Previously recovered alkali basaltic dredge samples from the uppermost summit of the seamount yielded K-Ar ages between 8 and 13 Ma [*Wendt et al.*, 1976]. Beginning in the north, the region can be divided into four geomorphic areas: (1) a WSW-ENE trending crest composed of the Teresa Seamount summits, (2) an accumulation of smaller seamounts and structures NE of Josephine (henceforth called Josephine North), (3) Josephine Seamount, and (4) Erik Seamount which is located 50 km SW of Josephine (Figure 1b).

[7] Volcanic rocks were recovered from all four areas during the M51/1 cruise. Evolved rocks containing feldspar phenocrysts and rare amphibole in a palagonitized matrix have been dredged from the deep NE slope of Teresa Seamount. Multibeam echosounding revealed a number of apparently young volcanic structures in the twin-peaked Josephine North area. Volcanic rock samples were retrieved from three sites (working names): Pico Julia, a 300 m high cone with a top at 1900 mbsl, Pico Pia, a 600 m high cone with a top in 1160 m water depth, and Toblerone Ridge, a 2.5 km long steep and narrow NNW-SSE oriented ridge in <2000 m depth, probably resulting from fissure eruptions. Most recovered rocks are vesicular lavas with olivine and minor clinopyroxene phenocrysts. Samples from all three sites are subangular to well rounded (cobbles), which may indicate former wave action and thus major subsidence [*Hoernle and Scientific Party*, 2003]. Welded spatter and

Table 2. The ^{40}Ar/^{39}Ar Step Heating Age Determinations and Single-Crystal Total Fusion Age data (403 DR-1)[a]

Sample	Location	Phase	Plateau Age/Mean Age, Ma	2 sigma	Plateau Steps n (of n)	Percent ^{39}Ar Plateau	MSWD
399 DR-1	JN (Pico Pia)	mx	0.52	±0.44	12 (20)	73.7	0.6
399 DR-1	JN (Pico Pia)	mx	0.88	±0.15	6 (20)	43.8	1.4
Weighted average			0.84	±0.16			
403 DR-1	Teresa Seamount	hbl	92.5	±0.40	-	-	1.4
403 DR-5	Teresa Seamount	hbl	94.5	±0.43	8 (20)	54.9	2.0
406 DR-7	JN (Toblerone Ridge)	gls	1.40	±0.60	12 (20)	82.8	0.7
406 DR-7	JN (Toblerone Ridge)	mx	0.46	±0.13	20 (20)	99.9	1.5
407 DR-4	JN (Pico Julia)	mx	6.98	±0.71	12 (20)	82.9	0.7
407 DR-4	JN (Pico Julia)	mx	7.39	±0.46	10 (20)	57.9	0.6
Weighted average			7.27	±0.43			
408 DR-2	Josephine Seamount	mx	15.84	±0.86	17 (20)	93.5	1.0
408 DR-2	Josephine Seamount	mx	13.62	±0.64	15 (20)	64.1	1.4
409 DR-1	Josephine Seamount	mx	11.58	±0.72	11 (20)	70.0	1.3
409 DR-1	Josephine Seamount	mx	11.42	±0.64	11 (20)	61.7	0.5
Weighted average			11.49	±0.48			
410 DR-4	Josephine Seamount	mx	13.15	±0.62	15 (20)	83.9	0.7
410 DR-4	Josephine Seamount	mx	12.94	±0.30	15 (20)	80.5	1.6
Weighted average			12.98	±0.27			
412 DR-2	Eric Seamount	mx	3.62	±0.32	11 (20)	80.8	1.7
429 DR-1	Dragon Seamount	mx	1.43	±0.42	18 (20)	99.4	0.9
429 DR-1	Dragon Seamount	mx	1.12	±0.20	7 (20)	55.2	0.6
Weighted average			1.18	±0.18			
431 DR-1	Dragon Seamount	mx	3.94	±0.30	17 (20)	97.5	1.3
M9C-173	Great Meteor Seamount	mx	17.32	±0.28	13 (20)	83.2	1.0

[a]Abbreviations are JN, Josephine North; mx, matrix; hbl, hornblende (amphibole); gls, glass; MSWD, mean squared weighted deviates.

cinder fragments (Pico Pia) and lapilli tuff samples (Pico Julia) are also consistent with subaerial and/or shallow water eruptions. Several fine-grained, quartz-bearing sandstones were recovered from a small canyon at the SE slope of the highest Josephine North Seamount. The sharp, freshly broken edges of the sampled blocks suggest that the sandstone outcrops on the canyon wall. In conclusion, these observations suggest that subsidence from sea level to the present sampling depths of ~1200–1900 m took place in this area.

2.2. Western Slope of the Madeira-Tore Rise

[8] The deeper parts of the MTR were sampled on the western slope at 4600 m water depths. The dredge contained volcanic rocks including lapilli tuffs and hyaloclastites containing basaltic clasts and carbonate rocks as well as extremely thick (20 cm) ragged manganese crusts. The olivine basalt clasts are vesicular (up to 20%) and are strongly altered (olivine phenocrysts totally iddingsitized, all vesicles filled with secondary phases) and were therefore excluded from geochemical investigations.

2.3. Southern Madeira-Tore Rise

[9] Lion Seamount, located near the southeastern flank of the MTR, is the highest structure in this area rising up to 600 mbsl. The eastern slope of Lion Seamount merges at water depths of ~3000 m with the western distal flank of Unicorn Seamount (located 110 km to the east of Lion Seamount), which belongs to the proposed Madeira hot spot track [Geldmacher et al., 2005]. Highly altered basaltic rock samples and volcanic breccias, both associated with consolidated carbonates, were obtained from the southern flank of Lion Seamount. The limestone samples, some of them in direct contact with the volcanic rocks, range from light yellowish gray mudstones to wackestones that are bioturbated and show several generations of bioerosion, such as

borings, which are filled by either lithified or unlithified calcareous sediment of apparently different ages.

[10] Dragon Seamount (rising to about 1500 mbsl) is located about 100 km SW of Lion Seamount and is the southwesternmost large seamount of the MTR before it declines to ~4000 m water depth and merges with the abyssal plain west of Madeira Island (Figure 1b). Well-preserved mafic volcanic rocks containing olivine, clinopyroxene and plagioclase phenocrysts were recovered from Dragon Seamount consistent with reports of previously dredged olivine basalts [Laughton et al., 1960].

3. Sample Preparation and Analytical Methods
3.1. The ^{40}Ar/^{39}Ar and Paleontological Age Determinations

[11] The ^{40}Ar/^{39}Ar incremental heating experiments were conducted on amphibole and matrix chips at the IFM-GEOMAR Tephrochronology Laboratory. The particles were hand-picked from crushed and sieved splits. All separates were cleaned using an ultrasonic disintegrator. Amphibole phenocrysts were then etched in 15% hydroflouric acid for 10 min. Samples were neutron irradiated at the 5-MW reactor of the GKSS Reactor Center (Geesthacht, Federal Republic of Germany), with crystals and matrix chips in aluminum trays and irradiation cans wrapped in 0.7 mm cadmium foil. Samples were heated by laser, either as single-step, total fusions of single amphibole phenocrysts, or by step-heating of single crystals and matrix chips. Purified gas samples were analyzed using a MAP 216 noble gas mass spectrometer. Raw mass spectrometer peaks were corrected for mass discrimination, background and blank values determined every fifth analysis. The neutron flux was monitored using TCR sanidine (Taylor Creek Rhyolite, 27.92 Ma [Dalrymple and Duffield, 1988; Duffield and Dalrymple, 1990]) and internal standard SAN6165
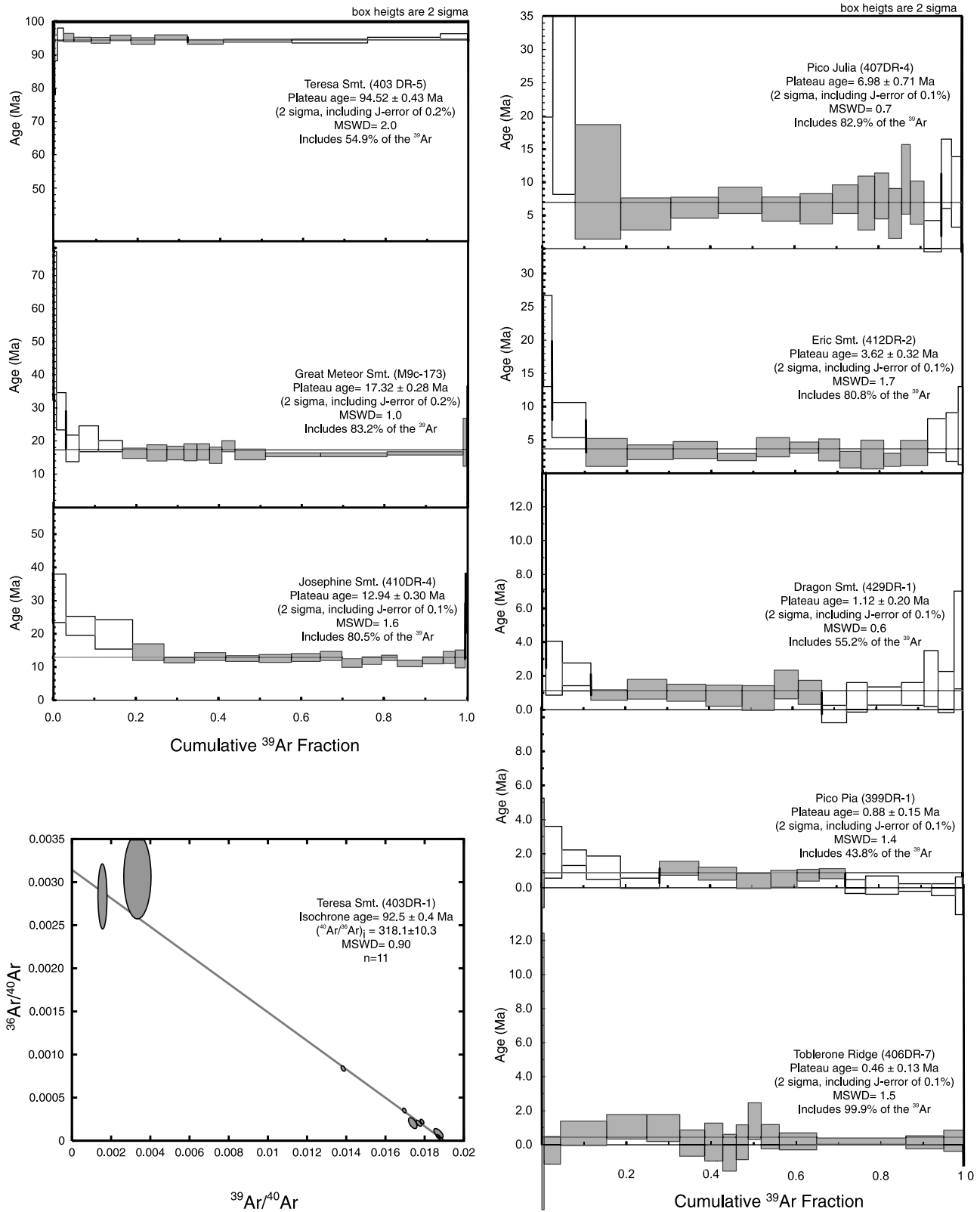
Figure 2. Age plateau (step heating) and isochron diagrams of representative samples from each seamount. Shaded boxes (2σ heights) indicate plateau steps included in the plateau age calculation. Error ellipses in isochron diagram are 1σ. See text for analytical details.

(0.470 Ma [*Bogaard*, 1995]). Vertical variations in J values were quantified by a cosine function fit. Lateral variations in J were not detected. Corrections for interfering neutron reactions on Ca and K are based on analyses of optical grade CaF_2 and high-purity K_2SO_4 salt crystals that were irradiated together with the samples. Eleven single crystals from sample 403DR-1 were dated in order to calculate mean apparent age and isochron age. Ages derived from step-heating analyses are based on plateau portions of the age spectra (Table 2). Plateau regions generally comprise > 50% of the ^{39}Ar released and 6–20 consecutive heating steps with ages within error (Figure 2). Sample 399DR-1 produced a smaller plateau (43.8%) but integrated ages and isochron ages identical within error. All errors in Table 2 are reported at the 2 sigma confidence level.

[12] Since the dredged volcanic rocks from the steep southern slope of Lion Seamount proved to be too altered for age determinations, associated limestone sediments were screened for microfossils to provide minimum ages for the underlying volcanic rocks. A split of sample number 421 DR-9 was crushed for microfossil analysis. Care was taken to avoid sampling of later stage infillings of borings. The material was dried in an oven, placed in a 50/50 mixture of ethanol and the tenside Rewoquat for several days, and the produced fine fraction washed over a $63 \mu m$ sieve. Because of the well-cemented nature of the limestone this procedure had to be repeated several times. The residual fraction yielded planktic foraminifera which have been identified from SEM micrographs.

3.2. Major and Trace Element Analyses

[13] After removal of altered outer surfaces, all samples were crushed and washed with deionized water in an ultrasonic bath and carefully hand-picked under a binocular microscope. Major elements and some trace elements (Co, Cr, Ni, V, Sr, Zr) were determined on fused beads by X-ray fluorescence spectroscopy (XRF) using a Phillips X'Unique PW 1480 with Rh tube at IFM-GEOMAR. H_2O and CO_2 were analyzed in an infrared photometer (Rosemount CSA 5003). International reference standards JB-2, JB-3, and JA-2, measured with the samples, gave major element accuracies better than 3% (SiO_2, TiO_2, Al_2O_3, MgO, K_2O, Na_2O, P_2O_5), 5% (Fe_2O_3, MnO, CaO), 7% (MnO) and trace element accuracies better than 3% (Sr), 5% (V), 12% (Ni), 18% (Zr), 20% (Co) and 41% (Cr).

[14] Analyses of trace elements (Sc, Cu, Zn, Ga, Rb, Y, Nb, Cs, Ba, Hf, Ta, Pb, Th, U, and all rare earth elements (REE)) were carried out on mixed acid (HF-aqua regia) pressure digestions which were prepared at 210°C using a MLS Ethos microwave and spiked with indium as an internal standard. About 50 mg of sample were processed and the final dilution factor was 1:5000 corresponding to 0.2 mg/mL of total dissolved solid. All analyses were carried out using a ThermoFinnigan Element2 inductively coupled plasma–mass spectrometer (ICP-MS) at the Institute of Geosciences, University of Bremen. To avoid mass interference, the REE and Hf were measured at high resolution (R = 10,000), the transition metals at medium (R = 4000) and all other elements at low (R = 300) resolution. Data were acquired in nine passes with dwell times between 0.12 and 2.4 s for each element. Repeated processing of U.S. Geological Survey (USGS) standards

(BCR-2) yielded external precision better than 5% for most elements and 11–17% for Nb and Ta. The accuracy of BCR-2 and BHVO-2 analyzed along with the samples is better than 5% except for Ga, Rb, Y, Pb, Th (<10%) and Cu, Hf, Ta (<15%) with respect to the USGS reference values.

3.3. Sr-Nd-Pb-Hf Isotope Geochemistry

[15] Sr-Nd-Pb isotope analyses were carried out on whole rock powders or rock chips on a ThermoFinnigan TRITION (Sr, Nd) and Finnigan MAT 262-RPQ2+ (Pb) thermal ionization mass spectrometers operating in static mode at IFM-GEOMAR. Samples were leached in 6 N HCL for ~1 hour at 120°C and dissolved in a hot 4:1 HF-HNO_3 mixture. Sr, Nd, and Pb chromatography followed the procedure outlined by *Hoernle and Tilton* [1991]. Sr and Nd isotope ratios were fractionation corrected within run to $^{86}Sr/^{88}Sr = 0.1194$ and $^{146}Nd/^{144}Nd = 0.7219$. Sr standard NBS 987 yielded 0.710257 ± 0.000010 (external 2 sigma error, n = 15). During two analysis periods NBS 987 yielded higher values of 0.710273 ± 0.000015 (n = 2) and 0.710283 ± 0.000026 (n = 3) and therefore data measured during these periods are normalized to 0.710257. Our in-house Nd SPEX monitor gave $^{143}Nd/^{144}Nd = 0.511711 \pm 0.000008$ (external 2sigma error, n = 18) corresponding to 0.511846 for the La Jolla standard. External reproducibility of replicate analyses for Sr and Nd isotopes is better than ± 0.000016. Analyses of Pb standard NBS 981 produced $^{206}Pb/^{204}Pb = 16.895 \pm 0.010$, $^{207}Pb/^{204}Pb = 15.431 \pm 0.011$, and $^{208}Pb/^{204}Pb = 36.508 \pm 0.037$ (2 sigma external errors, n = 19), resulting in an external reproducibility of 0.029%/amu. All Pb isotope analyses were fractionation corrected to the NBS 981 values of *Todt et al.* [1996]. Replicate analyses yielded an external reproducibility better than 0.03%/amu (2 sigma). Total Pb chemistry blank ranged between 19 and 53 pg and thus are considered insignificant.

[16] For all Hf isotope analyses, rock chips or powders (200–500 mg) were digested for 60 hours at 130°C on a hot plate using a mixture of about 10 mL 24 mol/L HF and 1 mL 14 mol/L HNO_3. Chemical separation followed the procedure of *Blichert-Toft et al.* [1997]. Hafnium isotope analyses were carried out in 0.1 mol/L HNO3 at IFM-GEOMAR using an AXIOM MC-ICP-MS (multiple collector inductively coupled plasma mass spectrometer) in static mode. A Cetac Aridus membrane desolvator in combination with Elemental Scientific PFA MicroFlow nebulizers were used for sample introduction. The Faraday collector array was set up identical to previous studies [e.g., *Blichert-Toft et al.*, 1997] to collect ion beams for ^{176}Hf, ^{177}Hf, ^{178}Hf, ^{179}Hf and ^{180}Hf together with ^{173}Yb, ^{175}Lu, ^{181}Ta and ^{182}W for interference corrections. All measured isotope ratios were corrected for instrumental mass discrimination relative to $^{179}Hf/^{177}Hf = 0.7325$ [*Patchett and Tatsumoto*, 1980] using the exponential mass fractionation law [*Russel et al.*, 1978]. Online interference corrections for Yb, Lu, Ta and W are applied to the "raw" Hf isotope ratios uncorrected for mass discrimination, to obtain interference corrected raw data for offline evaluation if needed. This procedure requires that the instrumental mass discrimination of the ICP-MS is mimicked for the natural Yb, Lu, Ta and W isotope ratios used for the interference corrections [e.g., *Thirlwall and Anczkiewicz*, 2004]. For this mass bias adjustment, the exponential law mass discrimination coefficient *f*, determined from the Hf

reference isotope ratio (f = ln $(0.7325/(^{179}\text{Hf}/^{177}\text{Hf})_{raw})$/ (mass^{179}Hf/mass^{177}Hf)), was applied to the natural Yb, Lu, Ta and W ratios. For example, $^{176}\text{Lu}/^{175}\text{Lu}_{mass\ bias\ adjusted}$ = $^{176}\text{Lu}/^{175}\text{Lu}_{natural}$ × (mass^{176}Lu/mass^{175}Lu)$^{-f}$.

[17] Uncertainties in the true isotope ratios of the interfering elements, the $^{179}\text{Hf}/^{177}\text{Hf}$ ratio and the slight difference in the instrumental mass discrimination exhibited by different elements [Maréchal et al., 1999] would result in small inconsistencies if large interference corrections were to be made. Therefore we determined the best $^{176}\text{Yb}/^{173}\text{Yb}$ and the $^{176}\text{Lu}/^{175}\text{Lu}$ for the interference corrections by comparison of Lu and Yb doped Hf standard solutions with Yb and Lu free runs [Ulfbeck et al., 2003; Thirlwall and Anczkiewicz, 2004]. Our best fit $^{176}\text{Lu}/^{175}\text{Lu}$ ratio, however, was almost identical to $^{176}\text{Lu}/^{175}\text{Lu}$ = 0.02656 used by Blichert-Toft et al. [1997], and this value was therefore adopted for the correction. The empirically determined $^{176}\text{Yb}/^{173}\text{Yb}$ = 0.7929, however, differs substantially from the previously suggested value ($^{176}\text{Yb}/^{173}\text{Yb}$ = 0.7876 [McCulloch et al., 1977]) used by Blichert-Toft et al. [1997] but is very similar to the empirically derived value of Ulfbeck et al. [2003]. Because Ta and W interfere only with ^{180}Hf which is not involved in the calculation of corrected $^{176}\text{Hf}/^{177}\text{Hf}$ values, $^{180}\text{Ta}/^{181}\text{Ta}$ = 0.0001198 [Weyer et al., 2002] and $^{180}\text{W}/^{182}\text{W}$ = 0.004501 [Lee and Halliday, 1995] were adopted from the literature without further attention. Yb and Lu interference corrections in this study were 21 ppm at maximum (one case) but usually well below (<15 ppm).

[18] Hafnium isotope ratios were analyzed for four blocks of 25 ratios each with a five second integration time and 30 second baseline measurements prior to each block 0.5 amu below the collected masses. Our in-house Spex Hf standard and/or the international JMC-475 Hf standard were run repeatedly every two or three samples to ensure consistent results throughout the measurement session. The JMC-475 Hf standard averaged 0.282126 ± 16 (2σ, n = 39) and 0.282125 ± 10 (2σ, n = 24) during two periods of analysis in 2004 and 2005 corresponding to a reproducibility of 58 and 34 ppm (2σ), respectively. The instrumental mass discrimination in MC-ICP-MS diverges slightly from the exponential law [Vance and Thirlwall, 2002; Wombacher and Rehkämper, 2003; Wieser and Schwieters, 2005], and Thirlwall and Anczkiewicz [2004] argued that true Hf isotope ratios will differ from exponential law corrected MC-ICP-MS data. This nonexponential law behavior and possible mass-independent fractionation effects [Albarède et al., 2004] such as slight variations in cup efficiencies (that were all set to 1 in this study) or imperfectly flat topped peaks are expected to result in slightly different normalized $^{176}\text{Hf}/^{177}\text{Hf}$ data from different instruments (and even different measurement sessions).

[19] To facilitate accurate comparison with other labs, an empirical correction factor is applied to our $^{176}\text{Hf}/^{177}\text{Hf}$ data in such a way that the average value of JMC 475 Hf measurements yields $^{176}\text{Hf}/^{177}\text{Hf}$ = 0.282163 [Blichert-Toft et al., 1997]. Following this adjustment, our in-house SPEX Hf standard (PLHF1-2X, Lot 9) yields an averaged, JMC 475-normalized $^{176}\text{Hf}/^{177}\text{Hf}$ of 0.282175 ± 15 (n = 65), and the international rock reference standard BHVO-1 (repeatedly digested and processed as outlined above) averaged 0.283112 ± 8 (n = 6) and 0.283104 ± 17 (n = 3). These

results agree within uncertainty with previously reported values of 0.283102 ± 10 and 0.283104 ± 9 [Ulfbeck et al., 2003] and of 0.283113 ± 10 [Le Fèvre and Pin, 2001].

4. Results

4.1. Age Determinations

[20] The $^{40}\text{Ar}/^{39}\text{Ar}$ incremental heating and single crystal analyses for 11 samples are presented in Table 1 and the results are summarized in Figure 1b. Where multiple analyses are within 2σ analytical error, the weighted averages are given. Representative age spectra (and one isochron) plots appear in Figure 2. The oldest ages of 94.5 ± 0.4 and 92.5 ± 0.4 Ma were obtained from amphibole separates from two different samples from Teresa Seamount. In contrast, samples from the Josephine North area gave very young ages of 0.8 ± 0.2 Ma (matrix sample, Pico Pia), 0.5 ± 0.1 and 1.4 ± 0.6 Ma (matrix and glass of one sample from Toblerone Ridge) and 7.3 ± 0.5 Ma (matrix sample, Pico Julia). Three matrix samples were analyzed from the southern slope of Josephine Seamount yielding ages between 11.5 ± 0.5 and 15.8 ± 0.9 Ma. These ages from the deeper flanks of Josephine Seamount extend the previously reported K-Ar age range of 8−13 Ma [Wendt et al., 1976] for samples from the top of Josephine (170− 400 mbsl), indicating that this volcano was active for at least 8 Myr (8−16 Ma). A matrix sample from nearby Erik Seamount was dated at 3.6 ± 0.3 Ma. Two matrix samples from the northern slope and summit of Dragon Seamount gave ages of 1.2 ± 0.3 and 3.9 ± 0.3 Ma.

[21] For comparison, a matrix sample from Great Meteor Seamount (M9/173) was analyzed as well and gave an age of 17.3 ± 0.3 Ma. This age is almost within error of the previously determined K-Ar age of 16.3 ± 0.4 Ma from this sample [Wendt et al., 1976].

[22] Within the limestone sediments from Lion Seamount, numerous specimens of eleven species of planktic foraminifera have been found, eight of which could be identified to species level: Archaeoglobigerina blowi Pessagno, Globigerinelloides prairiehillensis Pessagno, Globotruncana arca (Cushman), G. ventricosa White, Globotruncanita stuartiformis Dalbiez, Heterohelix globulosa (Ehrenberg), Pseudoguembelina costellifera Masters, and P. costulata (Cushman). Whereas most of these species range from at least Santonian through to late Maastrichtian, G. ventricosa and G. prairiehillensis have their first occurrence in the mid-Campanian (at the beginning of the normal chron in chronozone C33 and the planktic foraminiferal Zone G. ventricosa) and their last occurrence in the early Maastrichtian (at the end of the reversed chron in chronozone C31 and in the Gansserina gansseri Zone) [Caron, 1985; Robaszynski and Caron, 1995]. Whereas the last occurrence of P. costellifera is also in the G. gansseri Zone [Nederbragt, 1991], both G. ventricosa and P. costellifera occur only sporadically throughout this zone. Their common presence in the sample thus argues for an age of deposition of the limestone from mid to late Campanian, i.e., from circa 73 to 80 Ma [Premoli Silva and Sliter, 1999] and provides a minimum age for Lion Seamount of ∼80 Ma.

[23] The faunal dominance of planktic foraminiferas in the sample as well as the common occurrence of keeled taxa

Table 3. Major Element Concentration and Trace Elements[a]

	399 DR-1	399 DR-6	399 DR-10	406 DR-1	406 DR-7	407 DR-4	407 DR-5	M9/101a	M9/123	M9/129a	M9/133-3	408 DR-2	408 DR-3	409 DR-1
Location	Josephine North	Josephine North	Josephine North	Josephine North	Josephine North	Josephine North	Josephine North	Josephine Seamount	Josephine Seamount	Josephine Seamount	Josephine Seamount	Josephine Seamount	Josephine Seamount	Josephine Seamount
Type	basanite	basanite	basanite	basanite		basanite	basanite	alkali basalt	basanite	basanite	basanite	alkali basalt	alkali basalt	
SiO_2	40.8	41.0	40.9	43.4	nd	40.9	39.5	44.3	43.4	43.4	42.7	47.4	45.4	nd
TiO_2	3.26	3.18	3.06	3.29	nd	3.71	3.63	2.56	2.89	2.78	2.76	2.28	2.20	nd
Al_2O_3	13.9	12.9	12.8	14.6	nd	14.4	13.8	14.5	13.6	14.5	14.0	16.4	16.8	nd
Fe_2O_3t	13.3	13.6	13.1	13.2	nd	14.5	15.0	13.2	13.4	12.5	13.5	12.6	13.8	nd
MnO	0.18	0.18	0.17	0.18	nd	0.15	0.18	0.15	0.20	0.15	0.18	0.12	0.14	nd
MgO	8.17	9.79	9.82	6.93	nd	9.48	10.3	7.62	9.51	10.0	10.5	4.85	6.57	nd
CaO	11.1	11.4	11.8	10.6	nd	10.2	9.07	11.2	9.89	10.1	10.3	10.7	8.83	nd
Na_2O	3.74	3.55	3.46	3.85	nd	2.55	2.29	2.45	3.74	2.63	2.69	3.44	3.01	nd
K_2O	1.94	1.74	1.67	2.04	nd	0.98	0.94	1.02	1.09	0.90	1.13	0.50	0.71	nd
P_2O_5	1.10	0.99	1.00	0.67	nd	1.00	1.31	0.46	0.88	0.73	0.70	0.40	0.44	nd
CO_2	0.03	0.04	0.02	0.17	nd	0.10	0.16	0.45	0.05	0.11	0.22	0.05	0.10	nd
H_2O	1.35	1.34	1.19	2.11	nd	2.53	2.63	2.04	1.54	2.09	2.11	1.93	2.93	nd
LOI	1.38	1.38	1.21	2.28	nd	2.63	2.79	2.49	1.59	2.20	2.33	1.98	3.03	nd
Total	98.9	99.7	98.9	101.0		100.6	98.8	100.0	100.2	99.9	100.8	100.7	101.0	
V^b	282	266	264	272	nd	312	317	285	275	249	289	273	267	nd
Cr^b	123	186	209	214	nd	412	403	369	304	322	279	226	344	nd
Co^b	47	49	47	39	nd	57	77	48	53	48	55	32	51	nd
Ni^b	93	155	140	78	nd	218	303	143	206	240	221	87	174	nd
Sr^b	1290	1234	1204	1006	nd	1659	2660	500	899	820	671	396	355	nd
Zr^b	242	248	215	288	nd	291	256	179	305	250	239	157	146	nd
Sc	18.2	27.4	23.3	19.4	22.3	25.5	22.9	nd	22.8	nd	27.2	28.5	nd	41.9
Cu	49.9	54.5	42.5	56.0	55.7	43.8	62.9	nd	36.8	nd	57.7	77.5	nd	50.5
Zn	120	134	114	107	126	117	126	96[b]	143	117[b]	120	122	151[b]	93.7
Ga	19.9	23.1	18.1	22.8	21.1	19.0	16.0	17[b]	23.2	15[b]	21.1	23.5	16[b]	17.4
Rb	37.2	38.8	29.6	34.4	33.2	10.6	10.2	14[b]	15.1	17[b]	18.1	9.27	11[b]	12.7
Y	27.7	29.5	25.6	24.1	22.0	28.5	32.4	25[b]	30.3	27[b]	24.5	25.8	29[b]	21.0
Nb	nd	99.2	83.5	86.3	70.7	84.4	75.6	32[b]	75.3	63[b]	51.0	25.9	29[b]	30.4
Cs	0.50	0.28	0.38	0.58	0.39	0.08	0.06	nd	0.55	nd	0.08	0.68	nd	0.20
Ba	603	572	511	581	469	538	524	207[b]	503	419[b]	278	112	173[b]	207
La	92.4	90.2	82.6	59.9	45.6	54.9	54.6	<14[b]	57.7	<14[b]	37.1	18.8	<14[b]	18.4
Ce	179	183	164	113	90.8	113	103	26[b]	116	53[b]	77.5	38.4	24[b]	40.9
Pr	20.4	19.8	18.4	12.7	10.6	13.5	13.1	7[b]	13.1	5[b]	9.07	5.03	<4[b]	5.54
Nd	75.9	75.6	70.5	47.0	43.0	55.0	54.2	nd	54.9	nd	38.3	21.5	nd	24.8
Sm	12.4	12.2	11.5	8.98	8.59	10.8	10.3	nd	10.4	nd	7.81	5.61	nd	6.17
Eu	3.69	3.70	3.44	2.95	2.66	3.27	3.17	nd	3.31	nd	2.49	1.98	nd	2.01
Gd	9.84	9.91	9.23	7.85	7.65	8.69	9.25	nd	9.46	nd	7.24	5.83	nd	5.96
Tb	1.22	1.28	1.11	1.10	0.94	1.15	1.18	nd	1.27	nd	0.98	0.89	nd	0.83
Dy	6.69	6.66	6.33	5.58	5.35	6.45	6.82	nd	6.68	nd	5.60	5.27	nd	4.74
Ho	1.13	1.15	1.06	0.95	0.89	1.09	1.16	nd	1.15	nd	0.97	0.99	nd	0.86
Er	2.83	2.73	2.62	2.42	2.24	2.72	3.03	nd	2.85	nd	2.37	2.63	nd	2.14
Tm	0.35	0.35	0.33	0.31	0.27	0.33	0.40	nd	0.37	nd	0.31	0.35	nd	0.27
Yb	2.12	1.96	1.91	1.72	1.65	1.90	2.43	nd	2.20	nd	1.81	2.08	nd	1.61
Lu	0.31	0.27	0.27	0.24	0.23	0.26	0.34	nd	0.30	nd	0.23	0.29	nd	0.21
Hf	5.72	5.61	5.15	6.12	5.70	7.13	6.42	nd	7.13	nd	5.13	4.00	nd	4.58
Ta	nd	5.24	4.31	5.00	3.91	5.39	4.74	nd	4.45	nd	2.91	1.58	nd	1.99
Tl	ndt	ndt	ndt	0.18	ndt	0.09	0.19	nd	ndt	nd	ndt	0.07	nd	0.09
Pb	4.65	4.21	3.94	3.16	2.31	2.86	2.98	nd	3.07	nd	1.90	1.07	nd	1.22
Th	9.96	8.48	8.84	6.22	4.70	5.83	4.87	nd	5.35	nd	3.17	1.84	nd	1.87
U	2.86	2.54	2.52	1.97	1.54	1.96	2.65	nd	1.51	nd	0.93	0.51	nd	0.99

Table 3. (continued)

410 DR-2	410 DR-4	412 DR-2	412 DR-4	429 DR-1	429 DR-2	431 DR-1	403 DR-1	403 SR-1	391 DR-5	M9/173	M9/178TD	M9/178-5	JB-3	SD 2 sigma
Josephine Seamount	Josephine Seamount	Erik Seamount	Erik Seamount	Dragon Seamount	Dragon Seamount	Dragon Seamount	Teresa Seamount	Teresa Seamount	Ormonde Seamount	Meteor Seamount	Meteor Seamount	Meteor Seamount	standard (n = 5)	
alkali basalt	alkali basalt	basanite	picrite	alkali basalt	alkali basalt	hawaiite	trachyte	benmoreite	trachyte	alkali basalt	picrite	basanite		
42.4	46.1	43.4	40.2	45.8	46.7	49.6	59.9	57.0	64.3	46.3	40.5	39.4	50.9	0.24
2.55	2.71	2.39	2.36	2.45	2.67	2.35	1.07	1.06	0.28	3.14	4.66	3.81	1.41	0.02
13.4	16.9	13.5	11.8	14.2	15.6	16.1	19.2	21.4	18.2	13.0	12.7	13.8	17.4	0.08
10.9	13.1	13.8	13.9	12.9	12.6	11.7	4.23	4.67	2.30	12.7	14.6	14.5	11.9	0.06
0.14	0.16	0.18	0.17	0.16	0.16	0.19	0.17	0.04	0.18	0.16	0.14	0.14	0.17	0.00
10.4	4.23	11.5	16.4	9.49	5.95	3.81	0.92	0.92	0.22	10.2	8.41	7.71	5.23	0.12
13.5	10.5	10.5	10.1	10.5	11.3	8.33	3.24	2.82	0.51	8.98	12.5	11.6	9.76	0.04
2.38	3.55	2.61	1.44	2.97	3.41	4.48	5.77	5.50	7.36	2.84	2.14	2.28	2.77	0.14
0.86	0.96	0.85	0.33	0.85	1.08	1.66	4.93	2.73	5.54	1.28	0.66	0.58	0.77	0.02
0.43	0.82	0.50	0.67	0.51	0.50	0.64	0.20	0.22	0.07	0.59	0.73	0.61	0.30	0.02
2.24	0.11	0.04	0.08	0.05	0.00	0.04	0.02	0.08	0.01	0.05	0.97	2.04		
1.43	1.80	1.29	1.58	0.76	1.16	0.92	0.78	2.80	0.36	1.19	2.68	3.89		
3.67	1.91	1.33	1.66	0.81	1.16	0.96	0.80	2.88	0.37	1.24	3.65	5.93		
100.7	100.9	100.6	99.0		101.1	99.9	100.4	99.2	99.4	100.3	100.7	100.4		
278	310	278	273	271	284	237	29	34	17	261	335	324	383	7
459	258	498	784	357	140	193	<18	<18	<18	426	474	396	77	7
49	42	57	78	51	38	33	5	<4	<4	47	55	52	39	3
263	99	266	645	218	53	64	<2	<2	<2	298	186	219	40	4
494	479	556	701	501	560	902	892	1009	29	661	964	629	402	5
167	188	167	124	175	204	398	540	489	340	338	231	157	90	2
28.7	nd	27.4	27.8	25.9	nd	18.2	0.93	0.60	0.39	25.1	28.1	27.9		
65.4	nd	59.2	53.0	56.9	nd	40.4	1.71	7.53	2.08	45.9	46.3	65.2		
100	135[b]	95.8	117	114	113[b]	140	88.1	114	62.0	144	125	123		
18.1	23[b]	18.2	14.8	21.2	21[b]	27.1	21.4	22.0	23.3	22.8	20.3	20.3		
11.0	10[b]	13.7	7.05	13.5	12[b]	45.3	79.8	27.8	116	32.2	11.3	8.80		
20.3	40[b]	23.1	27.0	22.0	28[b]	31.9	31.7	12.9	22.8	27.0	24.6	22.2		
32.7	35[b]	36.1	35.5	34.2	36[b]	76.8	149	143	143	65.6	50.0	26.0		
0.13	nd	0.29	0.54	0.11	nd	0.33	0.34	0.32	0.66	0.08	0.43	0.33		
226	213[b]	252	217	223	266[b]	520	946	1096	523	307	325	167		
19.9	22[b]	27.5	27.7	24.9	<14[b]	65.1	79.2	37.5	175	47.9	29.3	17.1		
43.2	61[b]	54.6	53.6	51.0	51[b]	125	159	60.8	296	104	68.5	40.8		
5.62	5[b]	6.70	6.69	6.62	<4[b]	14.4	17.6	8.18	30.6	12.3	8.81	5.53		
24.8	nd	27.8	29.1	28.9	nd	59.3	65.6	31.2	91.3	52.1	40.7	27.0		
5.98	nd	6.33	6.59	6.81	nd	11.4	11.7	5.27	12.3	9.77	8.83	6.52		
1.96	nd	2.06	2.12	2.15	nd	3.49	3.65	2.84	2.58	3.04	2.95	2.33		
5.81	nd	5.93	6.52	6.27	nd	9.22	8.54	3.98	8.39	8.38	8.37	6.73		
0.80	nd	0.90	0.90	0.90	nd	1.30	1.22	0.57	1.15	1.15	1.10	0.92		
4.47	nd	5.02	5.46	4.94	nd	7.12	6.91	3.19	6.31	6.00	5.62	4.96		
0.83	nd	0.92	0.98	0.88	nd	1.25	1.26	0.60	1.02	1.07	0.98	0.87		
2.03	nd	2.51	2.69	2.23	nd	3.23	3.52	1.61	2.50	2.63	2.34	2.08		
0.27	nd	0.33	0.35	0.28	nd	0.43	0.49	0.24	0.32	0.33	0.29	0.26		
1.58	nd	1.95	2.31	1.61	nd	2.52	3.06	1.55	1.85	1.82	1.59	1.53		
0.22	nd	0.26	0.34	0.22	nd	0.35	0.46	0.24	0.23	0.26	0.21	0.20		
4.52	nd	4.20	4.34	4.81	nd	10.3	11.6	12.1	8.77	8.02	5.18	3.56		
2.13	nd	2.30	2.23	2.28	nd	5.08	8.38	8.88	13.7	4.05	3.15	1.66		
0.09	nd	0.16	ndt	0.15	nd	0.43	0.32	0.21	0.04	ndt	ndt	ndt		
1.30	nd	1.98	1.46	1.62	nd	4.39	7.33	5.39	7.98	2.37	1.29	0.74		
2.01	nd	2.92	2.96	2.79	5[b]	8.38	11.3	13.6	23.7	4.26	2.11	1.22		
0.81	nd	0.84	1.57	0.92	nd	2.15	0.83	0.70	0.58	1.30	0.65	0.78		

[a]Major element concentration are in wt %, and trace elements are in ppm. Trace element concentrations (except as indicated) were determined by ICP-MS. Abbreviations are ndt, not detected; nd, not determined.
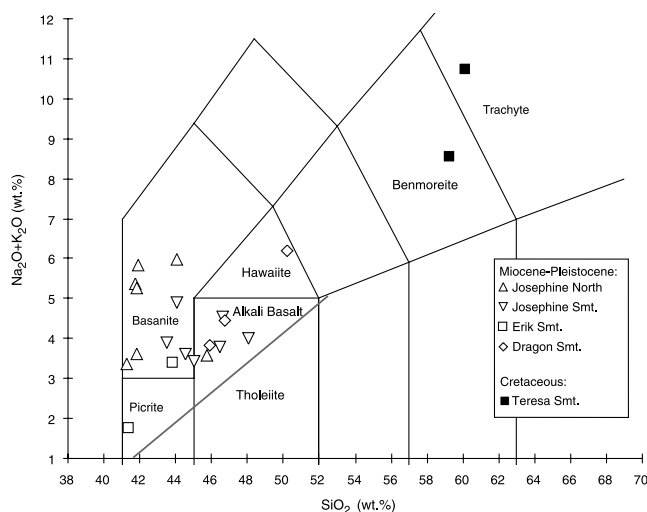[b]Determined by XRF.

Figure 3. Total alkalies versus silica diagram of MTR samples (data normalized to 100% on a volatile-free basis) after *Le Bas et al.* [1986].

(*Globotruncana, Globotruncanita*) implies a fully pelagic depositional setting [*Caron and Homewood, 1983*]. Furthermore, a location above the calcite compensation depth during deposition, which is placed at about 2700 to 3300 m in the North Atlantic during the Campanian [*Barrera and Savin*, 1999], is suggested by the predominantly unbroken nature of the planktic foraminifer tests [*Le and Shackleton*, 1992]

[24] In summary, radiometric and paleontological age determinations form two groups: (1) a Cretaceous group ($\sim$80$-$95 Ma) represented by samples from Teresa and Lion seamounts, and (2) a mid-Miocene to Pleistocene group (0.5$-$16 Ma) represented by Dragon, Josephine, and Erik seamounts and the nearby Josephine North volcanic field.

4.2. Major and Trace Elements

[25] All investigated volcanic MTR rocks have alkalic compositions (Table 3 and Figure 3). The Cretaceous samples from Teresa Seamount are the most evolved rocks, having benmoreitic and trachytic compositions. Trace element signature of trachytic sample 403DR-1 shows depletion in P, Ti and U and elevated Zr, Ba, K, Rb contents, reflecting advanced magmatic differentiation including crystal fractionation of apatite and Fe-Ti oxides (Figure 4a). Fractionation of U-rich, low Th/U phases such as apatite and titanite can explain the observed U, P and Ti depletions, which is also consistent with the concave down curvature of the REE pattern and relative Eu enrichment of Teresa 403 SR-1 sample (Figure 4b).

[26] The mid-Miocene to Pleistocene samples range from alkali basalt and hawaiite to picrite and basanite with samples from Josephine North being the most undersaturated (Figure 3). Similar to the Cretaceous samples, Miocene to Pleistocene MTR rocks display enrichments of the light relative to the heavy rare earth elements (La/Sm = 3.0$-$10.3, Ce/Yb = 18$-$93) consistent with residual garnet and/or clinopyroxene [*Blundy et al.*, 1998] in the mantle source. Furthermore, all MTR rocks are enriched in the high field strength elements (HFSE) Nb and Ta compared to K and Pb, a characteristic feature of high time-integrated U/Pb

(HIMU)-type ocean island basalts (OIB) [e.g., *Weaver*, 1991].

4.3. Isotope Ratios and Comparison With Madeira and Canary Compositions

[27] Volcanic rocks in the east Atlantic display a large range of isotopic compositions. On the basis of previous studies in the Madeira and Canary regions [e.g., *Hoernle et al.*, 1991; *Hoernle and Tilton*, 1991; *Geldmacher and Hoernle*, 2000; *Geldmacher et al.*, 2001, 2005; *Gurenko et al.*, 2006] isotopic compositions of OIB magmas east and southeast of the MTR can be grouped into two distinct isotopic domains: (1) a Madeira domain characterized by $^{87}Sr/^{86}Sr$ and $^{143}Nd/^{144}Nd$ isotope ratios overlapping Atlantic normal mid-ocean ridge basalt (NMORB) to a large extent but $^{207}Pb/^{204}Pb$ ratios plotting well below the North-
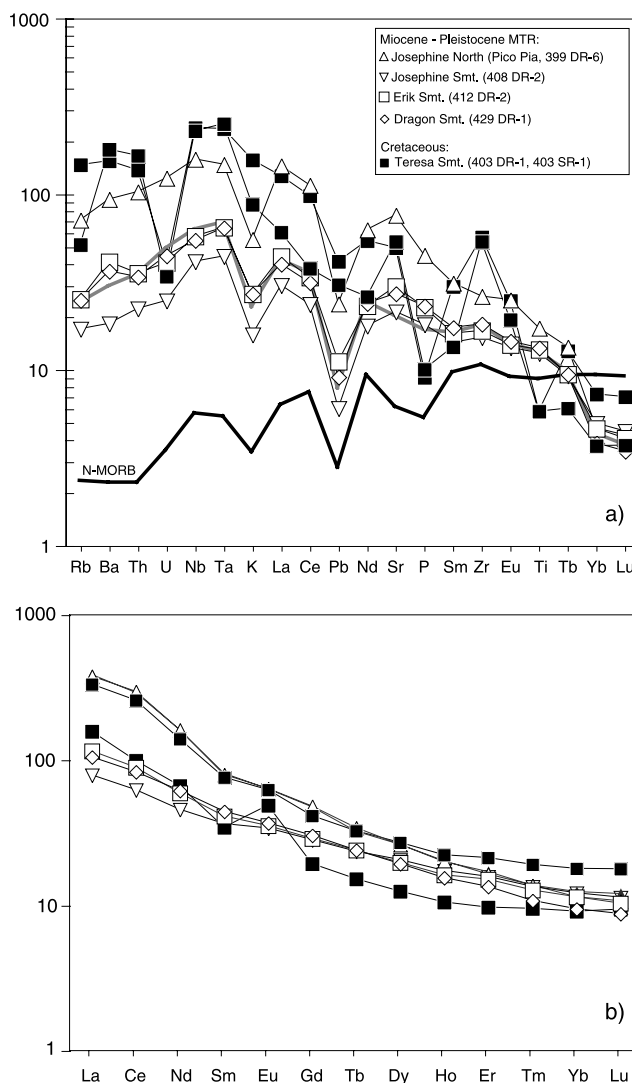

Figure 4. Multielement diagrams of representative Cretaceous and Miocene-Pleistocene MTR lavas normalized to (a) primitive mantle [*Hofmann*, 1988] and (b) C-1 chondrite [*Sun and McDonough*, 1989]. Solid black and gray lines show compositions of average NMORB [*Hofmann*, 1988] and HIMU ocean island basalt [*Chaffey et al.*, 1989], respectively.

Table 4. Pb, Sr, Nd, and Hf Isotope Ratios[a]

Sample	Location	$^{206}Pb/^{204}Pb$	$^{207}Pb/^{204}Pb$	$^{208}Pb/^{204}Pb$	$^{87}Sr/^{86}Sr$	$^{143}Nd/^{144}Nd$	ε Nd	$^{176}Hf/^{177}Hf$	ε Hf
	Madeira-Tore Rise								
403 DR-1	Teresa Seamount	19.660 (0)	15.594 (0)	39.632 (1)	0.703127 (3)	0.512942 (3)	5.93	0.282987 (8)	7.59
403 SR-1	Teresa Seamount	19.567 (1)	15.589 (1)	39.516 (1)	0.702991 (3)	0.512947 (3)	6.03	0.282982 (4)	7.41
399 DR-1	Josephine North (Pico Pia)	20.224 (1)	15.617 (1)	39.954 (2)					
399 DR-6	Josephine North (Pico Pia)	20.115 (7)	15.619 (6)	39.863 (15)	0.703238 (2)	0.512842 (2)	3.98	0.283011 (7)	8.46
399 DR-10	Josephine North (Pico Pia)	20.245 (2)	15.616 (1)	39.968 (4)	0.703231 (27)	0.512845 (2)	4.03	0.283004 (7)	8.19
406 DR-1	Josephine North (Toblerone Ridge)	19.706 (3)	15.574 (4)	39.349 (5)	0.703097 (3)	0.512925 (4)	5.60	0.283064 (6)	10.32
406 DR-7(g)	Josephine North (Toblerone Ridge)	19.560 (4)	15.568 (3)	39.189 (8)	0.703053 (3)	0.512952 (4)	6.12		
407 DR-4	Josephine North (Pico Julia)	19.860 (3)	15.582 (2)	39.530 (6)	0.704686 (3)	0.512895 (3)	5.02	0.283035 (6)	9.31
407 DR-4	Josephine North (Pico Julia)				0.703112 (3)[b]				
407 DR-5	Josephine North (Pico Julia)	19.859 (1)	15.591 (1)	39.555 (2)	0.705324 (3)	0.512902 (2)	5.15		
407 DR-5	Josephine North (Pico Julia)				0.703112 (2)[b]				
408 DR-2	Josephine Seamount	19.297 (4)	15.541 (3)	38.974 (7)	0.702907 (3)	0.513013 (3)	7.32	0.283091 (8)	11.28
408 DR-3	Josephine Seamount	19.313 (4)	15.548 (3)	38.990 (8)	0.702970 (3)	0.512996 (2)	6.99		
M9/123AT	Josephine Seamount	19.041 (1)	15.507 (0)	38.551 (1)	0.702922 (8)	0.513018 (4)	7.42		
M9/133-3	Josephine Seamount	18.866 (5)	15.495 (4)	38.461 (11)	0.702800 (5)	0.513055 (4)	8.13	0.283121 (7)	12.33
409 DR-1	Josephine Seamount	18.875 (4)	15.485 (4)	38.393 (8)	0.703090 (183)	0.513045 (3)	7.94		
410 DR-2	Josephine Seamount	18.914 (5)	15.500 (4)	38.430 (10)	0.702818 (3)	0.513045 (3)	7.93		
410 DR-4	Josephine Seamount	19.056 (2)	15.539 (2)	38.691 (4)	0.702913 (3)	0.513028 (3)	7.61		
412 DR-2	Erik Seamount	18.792 (4)	15.493 (4)	38.334 (8)	0.702972 (3)	0.513073 (2)	8.48	0.283163 (11)	13.84
421 DR-3	Lion Seamount	19.554 (1)	15.602 (1)	39.264 (2)	0.708099 (3)	0.512935 (2)	5.79	0.283028 (6)	9.06
421 DR-3	Lion Seamount				0.707834 (27)[b]				
429 DR-1	Dragon Seamount	18.888 (4)	15.497 (3)	38.414 (8)	0.702776 (3)	0.513090 (2)	8.81	0.283165 (6)	13.91
429 DR-2	Dragon Seamount	18.889 (2)	15.498 (2)	38.416 (5)	0.702766 (3)	0.513085 (2)	8.73		
431 DR-1	Dragon Seamount	19.004 (1)	15.507 (1)	38.529 (3)	0.702786 (3)	0.513084 (3)	8.69		
	Seamounts off the MTR								
391 DR-5	Ormonde Seamount	19.405 (1)	15.571 (0)	39.422 (1)	0.720170 (3)	0.512952 (2)	6.13	0.283033 (7)	9.24
391 DR-5	Ormonde Seamount				0.719506 (11)[b]				
M9/173	Great Meteor Seamount	19.822 (1)	15.590 (1)	39.352 (2)	0.703155 (6)	0.512886 (4)	4.84	0.282983 (8)	7.45
M9/178TD	Great Meteor Seamount	19.494 (2)	15.563 (2)	38.989 (5)	0.703199 (5)	0.512924 (4)	5.58	0.283036 (7)	9.33
M9/178-5	Great Meteor Seamount	19.400 (3)	15.557 (2)	38.861 (5)	0.703098 (5)	0.512952 (4)	6.13	0.283049 (8)	9.80

[a]All errors are 2 sigma. Abbreviation is (g), glass sample; εNd is calculated with $^{143}Nd/^{144}Nd_{CHUR}$ = 0.512638 and εHf is calculated with $^{176}Hf/^{177}Hf_{CHUR}$ = 0.282772 for present-day chondritic Earth.

[b]Leached in 80% 6 N HCL and 20% 3 N HNO_3 for 1 week at 120°C.

ern Hemisphere Reference Line (NHRL) and $^{206}Pb/^{204}Pb$ values extending to 19.8 and (2) a Canary domain with more radiogenic $^{87}Sr/^{86}Sr$, $^{206}Pb/^{204}Pb$ and $^{207}Pb/^{204}Pb$ isotope ratios but with less radiogenic $^{143}Nd/^{144}Nd$ ratios (<0.5130) than the Madeira domain.

[28] Sr, Nd, Pb, and Hf isotopes of representative MTR samples are presented in Table 4 and shown in Figures 5, 6, and 7. Clearly, there is no consistent affiliation of MTR volcanic rocks as a whole to either the Madeira or the Canary domain. The Cretaceous Teresa and Lion Seamount samples, however, plot consistently within the Canary domain field in all four diagrams. Both Cretaceous seamounts have slightly lower εHf values in respect to their εNd composition, showing the largest deviation from the global mantle array, compared to the mid-Miocene to Pleistocene MTR volcanic rocks.

[29] Since the Cretaceous samples are up to 95 Myr old, time-integrated growth of radiogenic isotopes needs to be considered. Because of the low U contents (see above) and the resulting low $^{238}U/^{204}Pb$ (μ = 7–8) and $^{235}U/^{204}Pb$ (0.005–0.006) values of Teresa samples, age correction of the measured $^{207}Pb/^{204}Pb$ and $^{206}Pb/^{204}Pb$ isotope data does not have any significant effect on the isotopic composition of these samples ($^{206}Pb/^{204}Pb_{in}$ = 19.44–19.55, $^{207}Pb/^{204}Pb_{in}$ = 15.58–15.59). Even if age correction is considered for the remaining isotope ratios ($^{208}Pb/^{204}Pb_{in}$ = 38.73–39.15, $^{87}Sr/^{86}Sr_{in}$ = 0.702797–0.702883 $^{143}Nd/^{144}Nd_{in}$ = 0.512878–0.512885 $^{176}Hf/^{177}Hf_{in}$ = 0.282976), Teresa Seamount (as well as Lion samples),
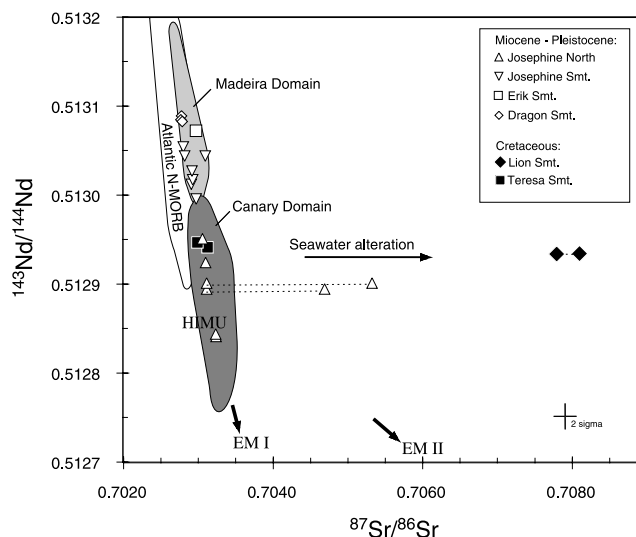
Figure 5. The $^{87}Sr/^{86}Sr$ versus $^{143}Nd/^{144}Nd$ ratios of MTR samples in comparison with compositional fields for the Madeira [*Geldmacher and Hoernle*, 2000] and Canary mantle domains [*Hoernle et al.*, 1991; *Hoernle and Tilton*, 1991; *Geldmacher et al.*, 2001; *Gurenko et al.*, 2006]. Elevated Sr isotope composition can be ascribed to seawater alteration. Stippled lines connect duplicate samples treated with different leaching methods (see Table 4). Even extensive leaching did not reduce further the $^{87}Sr/^{86}Sr$ ratio of the altered Lion Seamount sample.
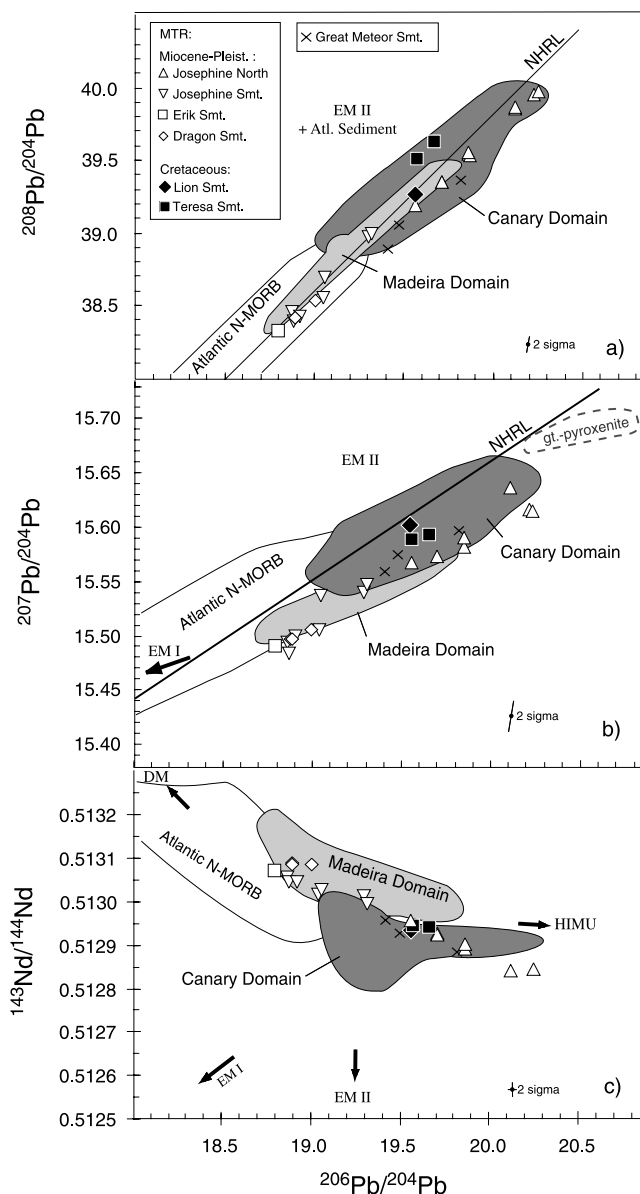
Figure 6. (a,b) Pb and Pb versus (c) Nd isotopic composition of MTR lavas. Cretaceous samples plot within the Canary domain whereas Miocene to Pleistocene rocks form a trend between the enriched end of the Canary field and the depleted end of the Madeira field or the NMORB field. NHRL, Northern Hemisphere Reference Line. Atlantic NMORB data between 10° and 30° are from the literature. See Figure 5 caption for additional references for the Madeira and Canary domains. Gt-pyroxenite data from Beni Bousera (Morocco) are from *Hamelin and Allègre* [1988].

tion. Beginning in the south, Erik and Dragon seamounts are isotopically most depleted (relatively unradiogenic Pb and radiogenic Nd isotope ratios) and overlap with the Madeira domain and Atlantic NMORB in Sr, Nd, Pb and Hf isotopic composition (Figure 5, 6, and 7). On the basis of their HIMU-like trace element characteristics, however, they can't be derived from a depleted NMORB source but could be potentially derived from the nearby Madeira hot spot. The youngest volcanic rocks on Madeira also have NMORB = type isotopic compositions and HIMU-type trace element compositions. Samples from Josephine Seamount show intermediate compositions. Josephine North samples, on the other hand, have the most enriched composition (radiogenic Pb and unradiogenic Nd isotope ratios: ^{206}Pb/^{204}Pb = 19.5–20.2; ^{143}Nd/^{144}Nd = 0.512842–0.512952) and overlap the Canary domain in all isotope systems. All MTR rocks lie below the Northern Hemisphere Reference Line (NHRL) in ^{206}Pb/^{204}Pb versus ^{207}Pb/^{204}Pb isotopic space (Figure 6b) and below the global Nd-Hf isotope mantle array (Figure 7).

[31] Three samples from Great Meteor Seamount, probably the largest seamount in the Atlantic and located about 1000 km to the SW of Madeira (Figure 1a), were also analyzed for comparison. These data are, to our knowledge, the first published Sr, Nd, Pb, and Hf isotope data from the 11–17 Ma Great Meteor Seamount [*Wendt et al.*, 1976; this study], which is believed to mark the end of the New England hot spot track [e.g., *Duncan*, 1984; *Tucholke and Smoot*, 1990]. All three samples show an enriched composition (^{206}Pb/^{204}Pb = 19.40–19.82, ^{143}Nd/^{144}Nd = 0.512886–0.512952) similar to the Canary domain
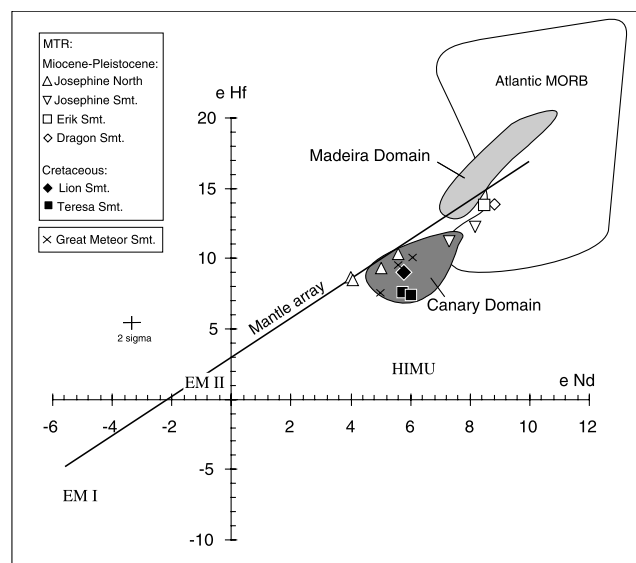
Figure 7. The εNd versus εHf isotope data from representative MTR lavas compared to the Madeira and Canary domains. As seen in Figure 6, Cretaceous samples plot within the Canary field, whereas Miocene to Pleistocene samples show a linear trend along the mantle array (heavy dark line, εHf = 1.4εNd + 2.8) between the enriched end of the Canary domain and NMORB or the Madeira field. Madeira and Canary domain fields are based on J. Geldmacher et al.'s unpublished data (2003).

projected to the present using assumed source parent-daughter ratios, would still plot within the Canary domain field in Sr, Nd, Pb, Hf isotopic space.

[30] In contrast to the few but widely spaced Cretaceous samples, the mid-Miocene to Pleistocene MTR volcanic rocks span a wide compositional range and form linear arrays on isotope correlation diagrams. In addition, isotopic compositions change systematically with geographic loca-

(Figures 6 and 7). Except for their slightly lower ^{208}Pb values, Great Meteor Seamount data agree relatively well with the few previously published Nd and Pb isotope data from the New England seamount chain ($^{206}Pb/^{204}Pb$ = 19.34–20.65, $^{207}Pb/^{206}Pb$ = 15.60–15.67, $^{143}Nd/^{144}Nd$ = 0.512789–0.512955, projected to present time [*Taras and Hart*, 1987]), thus supporting the idea of a common mantle source.

5. Discussion

5.1. Multiple Causes of Volcanism at the MTR?

[32] The new $^{40}Ar/^{39}Ar$ and paleontological ages presented here identify two major episodes of MTR volcanism: a Late Cretaceous and a mid-Miocene to Pleistocene episode. Rocks from the deepest parts of the MTR yield Late Cretaceous ages. Evidence for Miocene to Pleistocene volcanism, on the other hand, comes from along the entire MTR (Dragon, Erik, Josephine and Josephine North seamounts). Except for one dredge haul from the lower slope of Josephine Seamount (408 DR), all Miocene to Pleistocene rocks have been dredged at water depths above 2500 m from seamounts rising to summit heights of 150 m below sea level. Therefore it appears that the younger (mid-Miocene – Pleistocene) volcanic structures are superimposed on a much older, at least Late Cretaceous MTR basement.

5.2. Cause of Cretaceous MTR Volcanism

[33] The 93–95 Ma rock ages from deep dredge hauls (~3000 mbsl) at Teresa Seamount on the northern MTR and the ~80 Ma age inferred for Lion Seamount on the southern MTR imply that the MTR basement formed during Cretaceous times. Mid to Late Cretaceous ages between 80 and 104 Ma have also recently been obtained by U-Pb chronometry of zircon and titanite crystals from evolved rocks dredged in the northern part of the MTR (R. Merle et al., Cretaceous seamounts along the continent-ocean transition of the Iberian margin. U-Pb ages and Pb-Sr-Hf isotopes, submitted to *Geochimica Cosmochimica Acta*, 2006, hereinafter referred to as Merle et al., submitted manuscript, 2006). The U-Pb ages from Teresa Seamount ("Gago Couthino") agree within error with the $^{40}Ar/^{39}Ar$ ages presented here. Since the MTR covers the geomagnetic seafloor anomaly M 0 [e.g., *Klitgord and Schouten*, 1986] corresponding to crust formed at ~122 Ma, the Cretaceous MTR basement must have formed near the Mid-Atlantic spreading center. A genetic relation to the NNE-SSW oriented Atlantic spreading center is also suggested by the parallelism of the rise and the magnetic seafloor anomalies (Figure 1b).

[34] A Cretaceous age for the MTR basement is consistent with the gravity and elastic thickness models of *Peirce and Barton* [1991], suggesting that the MTR, or at least most parts of its volumetrically predominant pedestal, was formed contemporaneously with or soon after the underlying lithosphere. Thus the apparent contradiction between geophysical data and the few previously published Miocene K-Ar rock ages from Josephine summit can be explained by younger volcanic rocks having been erupted on an older and more voluminous Cretaceous rise. On the other hand, the large volume and the enriched trace element and isotopic composition of the recovered Cretaceous rocks are inconsistent with an origin from a normal MORB source at the Mid-Atlantic spreading center. Teresa and Lion samples plot well outside of the NMORB isotope fields (Figure 5, 6, and 7) and have OIB-like trace element and isotopic signatures. If we consider the geochemical composition of Teresa and Lion samples as representative for the entire MTR basement, this discrepancy can be explained by interaction of an enriched mantle plume with the Mid-Atlantic Ridge. It is striking that the Cretaceous MTR samples have isotopic compositions similar to the volcanic rocks from the Canary Islands. Therefore involvement of the Canary mantle plume in the formation of the MTR basement has to be evaluated in more detail.

[35] For any reconstruction of plume-ridge interaction in the North Atlantic, the apparent westward migration of the Mid-Atlantic spreading center has to be considered. Assuming fixed (or only slowly moving) plumes, all central Atlantic hot spots that are now located to the east of the Mid-Atlantic Ridge beneath the African plate, were west of the ridge beneath the American plate in mid-Cretaceous times [*Duncan*, 1984]. The complex pattern of seamount chains and plume-ridge interaction that develops when a spreading center overrides a hot spot has been modeled by *Sleep* [2002] and is illustrated in Figure 8.

[36] As the ridge approaches an intraplate (off-axis) hot spot, the lithospheric stress field becomes more and more compressive and plume material is increasingly ponded at the base of the lithosphere [*Sleep*, 2002]. The slope of the lithospheric base allows plume material to flow toward the ridge axis, and a ridge-centered hot spot to start at about the time when the off-axis activity ceases. The combined effect of this "hot spot capture" leads to a spatial gap in the hot spot track. Once the hot spot is ridge-centered, symmetric V-shaped tracks are formed on both plates (aseismic ridges, solid black lines in Figure 8a). Because of the plume flow toward the ridge axis, both aseismic ridges continue to form even after the plume is overridden by the migrating mid-ocean ridge. Not until the plume is far enough away from the ridge and below the new plate does lithospheric compression decrease and a distinct off-axis track begins to form, producing a second gap in the hot spot track (Figure 8b). Eventually the flow of plume material toward the ridge ceases and shuts off formation of the aseismic ridges at the spreading center. Subsequent seafloor spreading separates the aseismic ridges. The new hot spot track continues toward the SW with the active plume lying further and further to the south of the now isolated aseismic ridge (Figure 8c).

[37] The resulting hot spot tracks of this model are similar to the actual structural situation in the central east Atlantic (compare Figures 1a and 1b) except that not a single mantle plume but two closely neighboring plumes, Madeira and Canary hot spots, are proposed for this region [e.g., *Duncan*, 1984; *Geldmacher et al.*, 2001, 2005]. It appears therefore that the Cretaceous MTR basement could have formed as an aseismic ridge (solid black line to the right of the spreading center in Figure 8) during a period when the spreading center was above or near one of the two plumes. If this model is correct, a corresponding aseismic ridge should be located on the American plate (solid black line to the left of the spreading center in Figure 8). Indeed, a mirror
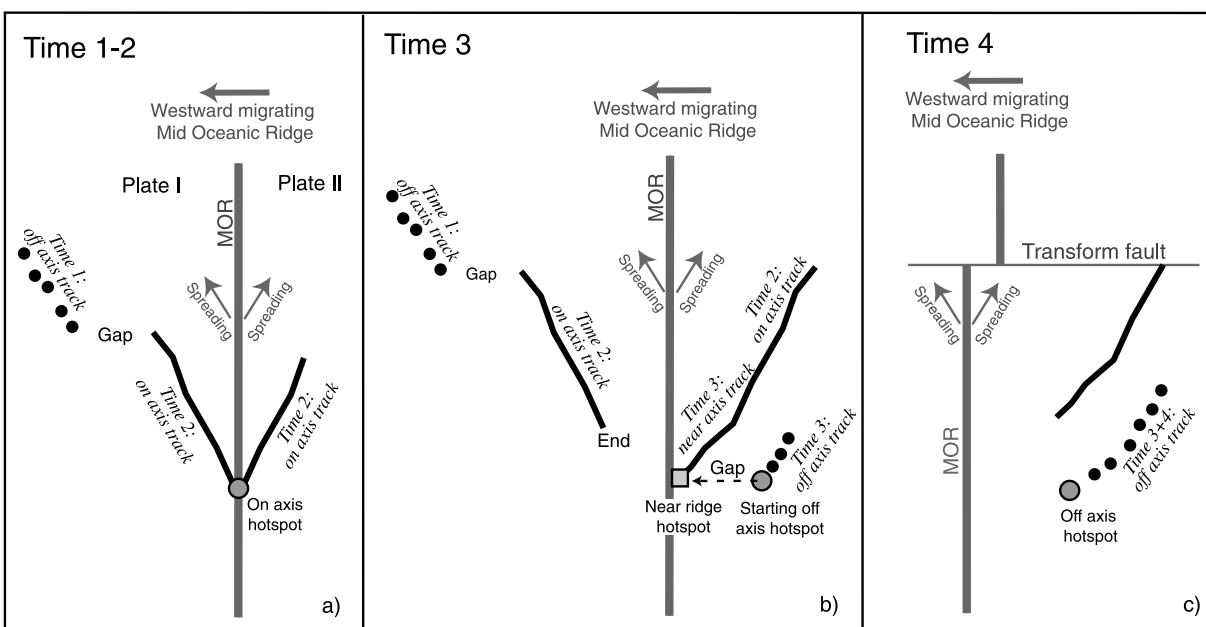
Figure 8. Schematic diagram of a ridge crossing plume track after *Sleep* [2002]. The position of the plume is shown as shaded circle. See text for details.

image rise, the J-Anomaly Ridge (JAR), is located south of the Grand Banks in the west Atlantic (Figure 1a). Like the MTR, it is associated with crust formed mainly during magnetic anomalies M-0 and M-1 (corresponding to the magnetic J-Anomaly) and is proposed to have formed by plume-ridge interaction [*Tucholke and Ludwig*, 1982; *Peirce and Barton*, 1991]. The available MTR basement age data suggest that the volcanism becomes younger toward the south (see also Merle et al., submitted manuscript, 2006) consistent with the aseismic ridge model. The JAR is covered by upper Barremian or lower Aptian carbonates [*Tucholke et al.*, 1979] and therefore a minimum age of ~117–124 Ma can be inferred. According to the model of *Sleep* [2002] an older overall age of the JAR relative to the averge MTR basement is expected because of the earlier separation and shut-off of the V-shaped ridge branch on the American side of the spreading center (JAR). In contrast, volcanism will persist longer along the aseismic ridge near the hot spot (MTR) on the African plate (see Figure 8b).

[38] The relatively young ages of Teresa Seamount (93–95 Ma), however, suggest a more complex origin of the MTR basement than shown by the general and simplified model outlined in Figure 8. The time difference between M 0 (122 Ma) and the oldest radiometrically dated age of Teresa Seamount approximates 27 Myr. Even if we extrapolate the suggested ultra slow Atlantic spreading rate of ~0.7–1.0 cm/yr at M anomalies times [*Srivastava et al.*, 2000; *Hopper et al.*, 2004], however, the volcanism occurred ~230 km away from the ridge axis. On the other hand, due to the sampling method by dredging it has to be assumed that the recovered rocks generally represent the youngest (latest) stages of volcanism at a given site. Therefore it is inferred that local volcanism persisted for some time (forming e.g., Lion and Teresa Seamount), even after the MTR was separated from the active spreading center and formation of the main body of the rise ceased.

This can be explained by the westward movement of the spreading center and the resulting long proximity of the MTR relative to the hot spot. Compared to the American plate (and the migrating spreading center), absolute African plate motion is slower in this region due to it's vicinity to the rotation pole (see, e.g., *Geldmacher et al.* [2005] for overview). Finally, the geochemically enriched composition of the Cretaceous MTR samples is consistent with the involvement of a mantle plume which, based on its distinct isotopic composition, is most likely the Canary plume.

[39] A similar model can be applied to the central Atlantic, connecting the New England seamount chain in the west Atlantic with the Corner Rise and Cruiser seamounts (probably relics of paired aseismic ridges now located on the American and African plates, respectively) and off-ridge Great Meteor Seamount (Figure 1a), the present location of the hot spot [e.g., *Sleep*, 1990].

[40] Alternatively, the Late Cretaceous volcanism could have been caused by widespread mantle upwelling in the central Atlantic. Such upwelling, however, is likely to produce large plateaus or scattered volcanism instead of elongated ridges and linear seamount chains elongated in the direction of plate motion (e.g., Fogo, Newfoundland, New England seamount chains) as observed in the North Atlantic (Figure 1a).

5.3. Toward a Comprehensive Geodynamic Reconstruction

[41] On the basis of the combined geochemical and age data, we now develop a comprehensive geodynamic model of the eastern central Atlantic since mid-Mesozoic times. Because of the close proximity of the Madeira and Canary hot spots it can be debated which one might have interacted with the early Mid-Atlantic spreading center to form the MTR. From the geochemical point of view, the few available basement samples from Cretaceous Teresa and Lion seamounts overlap with the compositional field for the
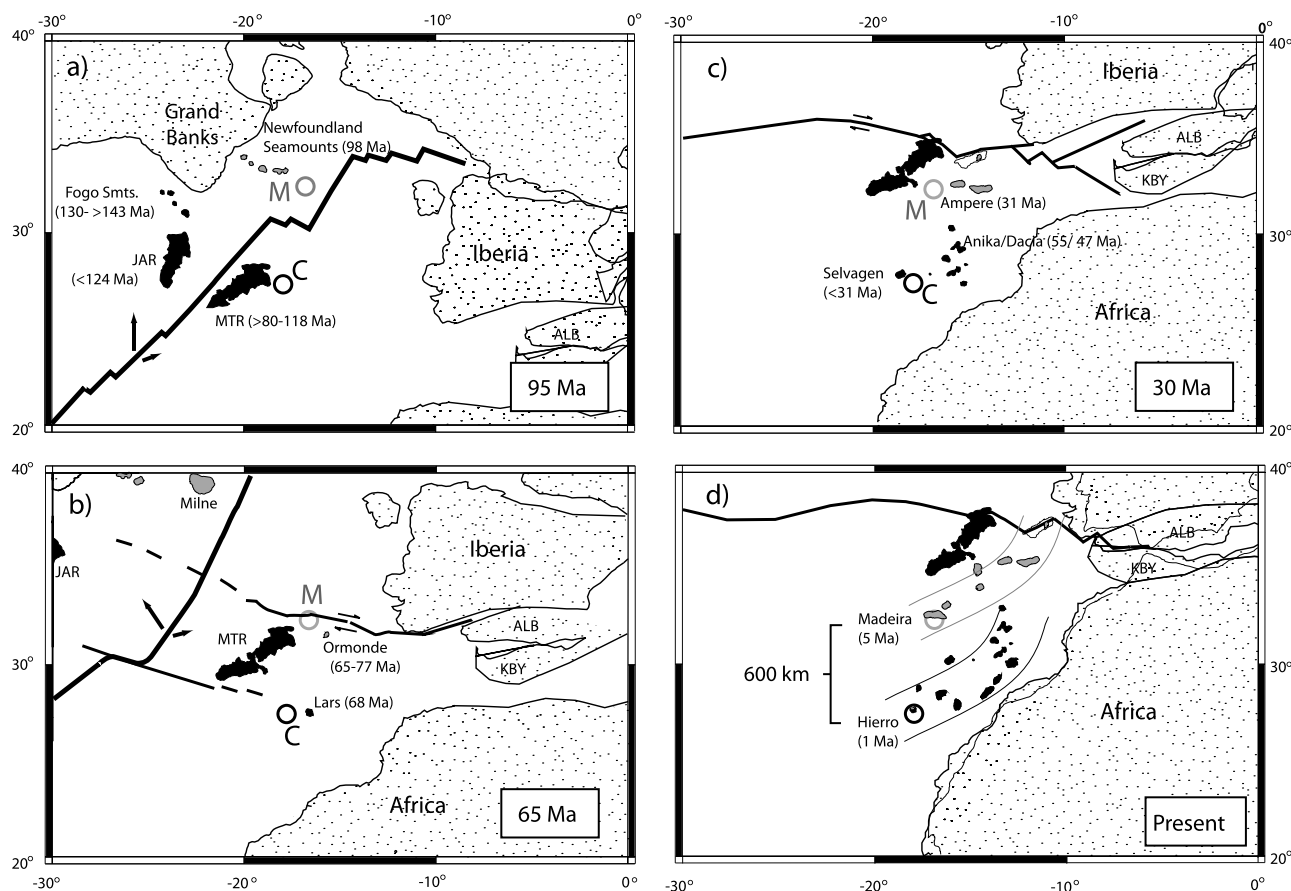
Figure 9. Plate tectonic reconstruction of continents after *Hay et al.* [1999] using the hot spot reference frame of *Cox and Hart* [1986]. Madeira (M, gray circle) and Canary (C, black circle) hot spots are kept fixed at present positions (at ∼600 km distance). Positions of seamounts and aseismic ridges are shown schematically. Volcanism assigned to the Madeira and Canary plumes is shown in gray and black, respectively. Age references are as follows: Fogo Seamounts, *Pe-Piper et al.* [2003]; Newfoundland Seamounts, *Sullivan and Keen* [1977] and *Srivastava et al.* [2000]; J-Anomaly Ridge, *Tucholke et al.* [1979] and *Tucholke and Ludwig* [1982]; Madeira-Tore Rise, this study; Ormonde Seamount, *Féraud et al.* [1982, 1986] and *Schärer et al.* [2000]; Lars Seamount, *Geldmacher et al.* [2001]; Anika and Dacia seamounts, *Geldmacher et al.* [2005]; Madeira, *Geldmacher et al.* [2000] and *Schwarz et al.* [2005]; and Hierro, *Guillou et al.* [1996]. The Madeira and Canary hot spot tracks shown in lower right figure (framed with stippled lines) are from *Geldmacher et al.* [2005]. Abbreviations of smaller continental blocks are ALB, Alboran Block, and KBY, Kabylia.

Canary plume in Sr, Pb, Nd, and Hf isotope space (Figure 5, 6, and 7). The initial Pb and Hf isotope data from feldspars and zircons from seamounts in the northern part of the MTR presented by Merle et al. (submitted manuscript, 2006) are also consistent with an origin from the Canary hot spot. Furthermore, in plate tectonic reconstructions the position of the Atlantic spreading center in the Mid-Cretaceous (e.g., *Hay et al.* [1999], using the hot spot reference frame of *Cox and Hart* [1986]) fits relatively well with the position of the Canary hot spot to allow the proposed plume-ridge interaction.

[42] During the early Cretaceous, the northward opening Atlantic broke Iberia apart from the Grand Banks of Newfoundland. If the Canary and Madeira hot spots already existed at that time [e.g., *Morgan*, 1983; *Duncan*, 1984], they were located beneath young, relatively thin oceanic crust after the Canadian continental shield passed over them. Since plume magmas readily penetrate young oceanic

crust, intraplate volcanism was initiated and formed two hot spot tracks. The Fogo seamount chain, located southwest of the Grand Banks, can be ascribed to the passage of the Canary hot spot: $^{40}Ar/^{39}Ar$ and paleontological age determinations of the alkaline and isotopically enriched Fogo seamounts range between 130 and >143 Ma and bathymetric data suggest an age progression of the chain, with younger seamounts to the SE consistent with a hot spot track [*Pe-Piper et al.*, 2003]. Because of its westward migration, the Atlantic spreading center moved over the Canary hot spot resulting in a gap in the hot spot track (compare Figure 8). The ridge-centered plume formed the JAR and MTR as paired aseismic ridges in the mid-Cretaceous. The JAR branch was separated first from the spreading center whereas the MTR locally continued to grow until ∼80–90 Ma due to the close proximity to the Canary hot spot being now located below the African plate (Figure 9a).

[43] In a similar way, the roughly E-W distributed, alkaline Newfoundland seamounts lie along the path of the Madeira hot spot [*Duncan*, 1984]. A $^{40}Ar/^{39}Ar$ age determination on plagioclase from one seamount from the central part of the chain yielded an age of 97.7 ± 1.5 Ma [*Sullivan and Keen*, 1977]. Even earlier activity of the Madeira plume may be represented by 115–145 Ma alkaline intrusions along the northeast coast of Newfoundland [*Duncan*, 1984]. In contrast to the Canary plume, the Madeira plume is proposed to be much weaker and is only intermittently active [*Geldmacher et al.*, 2000], which may explain the lack of a prominent V-shaped aseismic ridge when the Atlantic spreading center passed over it. On the other hand, the irregular shaped rise of the Milne seamount group (Figure 1a), separated by a ∼150 km broad gap from the easternmost Newfoundland Seamount, could represent a remnant of a small aseismic ridge. The lack of available age and geochemical data, however, makes this interpretation highly speculative.

[44] After termination of the aseismic ridge formation at the end of the Cretaceous, both hot spots continued to form the Madeira and Canary hot spot tracks, which are separated from the Mid-Atlantic spreading center by spatial gaps (Figure 9b). The Madeira hot spot produced alkaline volcanism near the Azores-Gibraltar fracture zone forming parts of Ormonde Seamount at around 70 Ma. The onset of the Canary hot spot track near Lars Seamount occurred at a similar time [*Holik et al.*, 1991; *Geldmacher et al.*, 2001, 2005]. Both hot spot tracks continued throughout the Cenozoic (Figures 9c and 9d), forming short, curved tracks resulting from the slow average Cenozoic rotation of the African plate of about 1.2 cm/yr in this region around an Euler pole migrating from a position south of Newfoundland to the southern tip of Greenland [e.g., *Geldmacher et al.*, 2005].

[45] The new and published age data for individual volcanic centers of both hot spot tracks generally agree well with geodynamic models such as shown in Figure 9. Minor discrepancies (particular at the early stages), however, can be due to uncertainties of the reconstruction models and chosen hot spot reference frames and to a number of additional factors, e.g., lack of precise ages for the oldest onset of volcanism at a given site, deflection of upwelling plume material in the upper mantle by convective currents [e.g., *Farnetani and Samuel*, 2005], or of ascending melts by lithospheric structures (see *Geldmacher et al.* [2005] for more detailed discussion). Furthermore, it has been shown that even prominent hot spots (such as Hawaii or Easter) are not absolutely fixed in the mantle but can drift [e.g., *Steinberger and O'Connell*, 1998; *Steinberger*, 2002; *Tarduno et al.*, 2003; *Parés and Moore*, 2005]. Considering all these uncertainties, the agreement between the observations and our model is reasonable.

5.4. Cause of Miocene to Pleistocene MTR Volcanism

[46] All young volcanic structures on the northern part of the MTR lie at, or in close proximity to, the active Azores-Gibraltar fault zone system. Plate kinematics and studies of earthquake fault plane solutions show that the tectonic regime east of the MTR is generally compressive resulting in underthrusting of the African plate and uplift of lithospheric blocks such as Gorringe Bank and Hirondel along

steep reverse faults [*Kaz'min et al.*, 1990]. Near Josephine Seamount, however, the strike of the right lateral strike-slip fault system turns from approximately WSW-ENE west of the MTR toward NW-SE at the northern end of the MTR before turning back to WSW-ENE at Hirondel and Gorringe Bank seamounts [e.g., *Jiménez-Munt and Negredo*, 2003] (Figure 1b). Therefore the development of local "pull-apart basin"-like lithospheric extension zones are inferred in the vicinity of Josephine Seamount, which is consistent with the sedimentological and volcanological evidence for major subsidence in the Josephine North area (see section 2.2). If subaerial or shallow eruption depth at Pico Pia and Toblerone Ridge are assumed, minimum average subsidence rates of 1–2 mm/yr can be estimated. Lithospheric thinning related to extension and pull-apart basin formation can lead to asthenospheric upwelling and small degree pressure-release melting beneath the base of the lithosphere.

[47] The mid-Miocene to Pleistocene volcanism on the MTR forms two-component mixing arrays on isotope correlation diagrams with the northernmost volcanics representing the enriched end-member and the southern volcanic rocks forming the depleted end-member. We envisage two alternative scenarios to explain the OIB-type trace element and enriched isotopic composition of the Josephine North and some Josephine Seamount volcanic rocks. The upwelling asthenosphere below the AGFZ may contain pyroxenitic material with enriched trace element and HIMU-type isotopic compositions, possibly representing recycled oceanic crust. *Hamelin and Allègre* [1988] reported Pb isotope ratios from garnet pyroxenite layers within the Moroccan lherzolite massif of Beni Bousera with $^{206}Pb/^{204}Pb$ ratios up to 20.8 placing them below the NHRL (Figure 6b). Preferred melting of a pyroxenitic component, being more fusible than mantle peridotite during low-degree partial melting, could serve as possible end-member for the Pb isotope enriched alkalic samples [e.g., *Hirschmann et al.*, 2003; *Kogiso et al.*, 2004].

[48] Alternatively, the enriched trace element and Canary-type Pb isotopic compositions could be derived from melting of the lithosphere beneath the MTR, overprinted by the Cretaceous Canary plume. During the slow passage of the lithosphere over the plume, the lithospheric mantle became metasomatized by plume melts and thus enriched. Since such trapped melts are enriched in incompatible elements relative to their mantle plume source, time integrated radiogenic growth of U and Th over the last >90 Myr could explain the more radiogenic Pb isotope enrichment of the Josephine North lavas slightly exceeding those of the present-day Canary lavas. Upwelling of hotter, deeper asthenosphere due to lithospheric extension and thinning along the Azores-Gibraltar Fracture Zone could have generated low degrees of melting of this fertile material at the base of the lithosphere. The different degrees of isotopic enrichment from the Josephine North volcanic fields to Josephine Seamount could reflect either various portions of available trapped Canary plume material (resulting in various mixing with more depleted sources) or differential extraction of such material, depending on the degree of melting. This is supported by the distinct correlation of $^{206}Pb/^{204}Pb$ isotope ratios of the mid-Miocene to Pleistocene MTR lavas with ratios of more to less incompatible trace element ratios such as Ce/Yb and La/Sm (Figure 10).
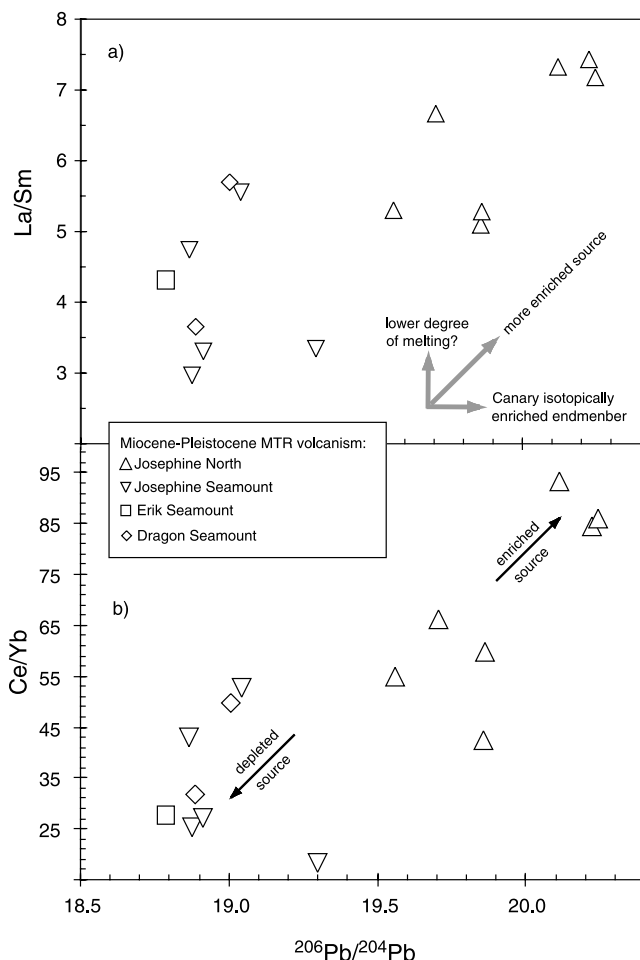
Figure 10. Positive trends of $^{206}Pb/^{204}Pb$ versus incompatible element ratios such as (a) La/Sm and (b) Ce/Yb formed by Miocene-Pleistocene MTR samples that are consistent with increasing isotopic enrichment due to lower degree of melting (higher portion of melts from more fertile, enriched components) or through mixing of enriched (Canary) and more depleted (Madeira) compositions.

[49] In contrast, the Pliocene-Pleistocene Dragon and Erik Seamount lavas on the southern and central MTR have enriched trace element but depleted Sr, Nd, Pb and Hf isotopic compositions similar to late stage volcanic rocks on Madeira Island and thus may be related to the Madeira hot spot. Dragon and Erik Seamount volcanism could have been caused either by melting of upwelling plume material on the distant margins of the Madeira plume or through melting at the base of the lithosphere under the MTR, related to upwelling of Madeira plume material. Since the central and southern part of the MTR passed closer to the Madeira hot spot than the northern part, as is illustrated by the proximity of Unicorn Seamount to MTR's Erik and Dragon seamounts (Figure 1b), the base of the southern MTR lithosphere could have been overprinted by the margin of the Madeira plume.

[50] In conclusion, the linear arrays formed by the Miocene-Pleistocene MTR volcanic rocks may reflect interaction of the Madeira plume material (from the margin of the Madeira plume or detached from the lithosphere beneath the

southern MTR) with enriched pyroxenitic material in the asthenosphere or lithosphere overprinted by Cretaceous Canary plume material beneath the northern MTR.

6. Conclusions

[51] Enriched isotopic and trace element compositions of Cretaceous MTR lavas are distinct from the composition of lavas from the Madeira mantle plume but are consistent with derivation from the Canary mantle plume. It is therefore proposed that the basement of the MTR originated by interaction of the Canary hot spot with the Mid-Atlantic spreading center and represents one branch of a paired aseismic ridge. As implied by radiometric and paleontological data, formation of the MTR continued locally until the Late Cretaceous when the rise was already separated from the spreading center. The MTR was subsequently modified by Cenozoic tectonic deformation and associated volcanism. Superimposed Miocene to Pleistocene volcanism on the northern MTR could be related to regional extension near the Azores Gibraltar fracture zone. The enriched geochemical composition of the Miocene to Pleistocene melts could be explained either by melting of enriched pyroxenitic material in the asthenosphere or Cretaceous Canary plume material underplated at the base of the lithosphere beneath the MTR. Isotopically depleted Pliocene to Pleistocene volcanism at the southern MTR, on the other hand, is isotopically similar to and thus probably related to the nearby Madeira plume.

References

Albarède, F., P. Telouk, J. Blichert-Toft, M. Boyet, A. Agranier, and B. Nelson (2004), Precise and accurate isotopic measurements using multiple-collector ICPMS, *Geochim. Cosmochim. Acta*, 68, 2725–2744.

Barrera, E., and S. M. Savin (1999), Evolution of late Campanian–Maastrichtian marine climates and oceans, in *Evolution of the Cretaceous Ocean-Climate System*, edited by E. Barrera and C. C. Johnson, *Spec. Pap. Geol. Soc. Am.*, 332, 245–282.

Blichert-Toft, J., C. Chauvel, and F. Albarede (1997), Separation of Hf and Lu for high-precision isotope analyses of rock samples by magnetic sector-multiple collector ICP-MS, *Contrib. Mineral. Petrol.*, 127, 248–260.

Blundy, J. D., J. A. C. Robinson, and B. J. Wood (1998), Heavy REE are compatible in clinopyroxene on the spinel lherzolite solidus, *Earth Planet. Sci. Lett.*, 160, 493–504.

Bogaard, P. v. d. (1995), $^{40}Ar/^{39}Ar$ ages of sanidine phenocrysts from Laacher See tephra (12,900 yr BP): Chronostratigraphic and petrological significance, *Earth Planet. Sci. Lett.*, 133, 163–174.

Caron, M. (1985), Cretaceous planktic foraminifera, in *Plankton Stratigraphy*, edited by H. M. Bolli, J. B. Saunders, and K. Perch-Nielsen, pp. 17–86, Cambridge Univ. Press, New York.

Caron, M., and P. Homewood (1983), Evolution of early planktic foraminifers, *Mar. Micropaleontol.*, 7, 453–462.

Chaffey, D. J., R. A. Cliff, and B. M. Wilson (1989), Characterization of the St. Helena source, in *Magmatism in the Ocean Basins*, edited by A. D. Saunders and M. J. Norry, *Geol. Soc. Spec. Publ.*, 42, 257–276.

Closs, H., G. Dietrich, G. Hempel, W. Schot, and E. Seibold (1968), Atlantische Kuppenfahrten 1967 mit dem Forschungsschiff Meteor, *Meteor Forschungsergeb., Reihe A*, 5, 71.

Cox, A., and R. B. Hart (1986), *Plate Tectonics: How It Works*, Blackwell Sci., Malden, Mass.

Dalrymple, G. B., and W. A. Duffield (1988), High precision $^{40}Ar/^{39}Ar$ dating of Oligocene tephra from the Mogollon-Datil volcanic field using a continuous laser system, *Geophys. Res. Lett.*, 15, 463–466.

Duffield, W. A., and G. B. Dalrymple (1990), Taylor Creek rhyolite of New Mexico, a rapidly emplaced field of domes and flows, *Bull. Volcanol.*, 52, 475–487.

Duncan, R. A. (1984), Age progressive volcanism in the New England Seamounts and the opening of the central Atlantic Ocean, *J. Geophys. Res.*, 89, 9980–9990.

Eckhard, F. J., P. Müller, and H. Raschka (1977), Geochemische und petrologische Untersuchungen an Basalten der Meteor-Kuppenfahrt (Mittlerer Atlantik) (abstract), *Fortschr. Mineral.*, 54, 115.

Farnetani, C. G., and H. Samuel (2005), Beyond the thermal plume paradigm, *Geophys. Res. Lett.*, 32, L07311, doi:10.1029/2005GL022360.

Féraud, G., J. Gastaud, J.-M. Auzende, J.-L. Olivet, and G. Cornen (1982), $^{40}Ar/^{39}Ar$ ages for alkaline volcanism and the basement of Gorringe Bank, North Atlantic Ocean, *Earth Planet. Sci. Lett.*, 57, 211–226.

Féraud, G., D. York, C. Mével, G. Cornen, C. M. Hall, and J.-M. Auzende (1986), Additional $^{40}Ar/^{39}Ar$ dating of the basement and the alkaline volcanism of Gorringe Bank (Atlantic Ocean), *Earth Planet. Sci. Lett.*, 79, 255–269.

Geldmacher, J., and K. Hoernle (2000), The 72 Ma geochemical evolution of the Madeira hotspot (eastern North Atlantic): Recycling of Palaeozoic (≤500 Ma) oceanic crust, *Earth Planet. Sci. Lett.*, 183, 73–92. (Corrigendum, *Earth Planet. Sci. Lett.*, 186, 333, 2001.)

Geldmacher, J., P. van den Bogaard, K. Hoernle, and H. Schmincke (2000), The $^{40}Ar/^{39}Ar$ age dating of the Madeira Archipelago and hotspot track (eastern North Atlantic), *Geochem. Geophys. Geosyst.*, 1(2), doi:10.1029/1999GC000018.

Geldmacher, J., K. Hoernle, P. v. d. Bogaard, G. Zankl, and D. Garbe-Schönberg (2001), Earlier history of the ≥70-Ma-old Canary hotspot based on the temporal and geochemical evolution of the Selvagen archipelago and neighboring seamounts in the eastern North Atlantic, *J. Volcanol. Geotherm. Res.*, 111, 55–87.

Geldmacher, J., K. Hoernle, P. v. d. Bogaard, S. Duggen, and R. Werner (2005), New $^{40}Ar/^{39}Ar$ age and geochemical data from seamounts in the Canary and Madeira volcanic provinces, *Earth Planet. Sci. Lett.*, 237, 85–101.

Guillou, H., J. C. Carracedo, F. Perez Torrado, and E. Rodriguez Badiola (1996), K-Ar ages and magnetic stratigraphy of a hot spot-induced, fast grown ocean island: El Hierro, Canary Islands, *J. Volcanol. Geotherm. Res.*, 73, 141–155.

Gurenko, A. A., K. A. Hoernle, F. Hauff, H.-U. Schmincke, D. Han, Y. N. Miura, and I. Kaneoka (2006), Major, trace element, Nd-Sr-Pb-O-He-Ar-Ne isotope signatures of shield stage lavas from the central and western Canary Islands: Insights into mantle and crustal processes, *Chem. Geol.*, 233, 75–112.

Hamelin, B., and C. J. Allègre (1988), Lead isotope study of orogenic lherzolite massifs, *Earth Planet. Sci. Lett.*, 91, 117–131.

Hay, W. W., et al. (1999), Alternative global Cretaceous paleogeography, in *The Evolution of Cretaceous Ocean/Climate Systems*, edited by E. Barrera and C. Johnson, *Spec. Pap. Geol. Soc. Am.*, 332, 1–47.

Hirschmann, M. M., T. Kogiso, M. B. Baker, and E. M. Stolper (2003), Alkalic magmas generated by partial melting of garnet pyroxenite, *Geology*, 31, 481–484.

Hoernle, K., and Scientific Party (2003), Cruise report M51/1, in *Meteor-Berichte 03-1*, edited by C. Hemleben et al., pp. 3–35, Univ. Hamburg, Hamburg, Germany.

Hoernle, K., and G. Tilton (1991), Sr-Nd-Pb isotope data for Fuerteventura (Canary Islands) basal complex and subaerial volcanics: Application to magma genesis and evolution, *Schweiz. Mineral. Petrogr. Mitt.*, 71, 5–21.

Hoernle, K., G. Tilton, and H.-U. Schmincke (1991), Sr-Nd-Pb isotopic evolution of Gran Canaria: Evidence for shallow enriched mantle beneath the Canary Islands, *Earth Planet. Sci. Lett.*, 106, 44–63.

Hofmann, A. W. (1988), Chemical differentiation of the Earth: The relationship between mantle, continental crust, and oceanic crust, *Earth Planet. Sci. Lett.*, 90, 297–314.

Holik, J. S., P. D. Rabinowitz, and J. A. Austin (1991), Effects of the Canary hotspot volcanism on structure of oceanic crust off Morocco, *J. Geophys. Res.*, 96, 12,039–12,067.

Hopper, J. R., T. Funck, B. E. Tucholke, H. C. Larsen, W. S. Holbrook, K. E. Louden, D. Shillington, and H. Lau (2004), Continental breakup and the onset of ultraslow seafloor spreading off Flemish Cap on the Newfoundlamd rifted margin, *Geology*, 32, 93–96.

Intergovernmental Oceanographic Commission, International Hydrographic Organization, and British Oceanographic Data Centre (1994), *GEBCO Digital Atlas*, Br. Oceanogr. Data Center, Birkenhead, UK.

Jiménez-Munt, I., and A. M. Negredo (2003), Neotectonic modeling of the western part of the African-Eurasia plate boundary: From the Mid-Atlantic Ridge to Algeria, *Earth Planet. Sci. Lett.*, 205, 257–271.

Jiménez-Munt, I., M. Fernandez, M. Torne, and P. Bird (2001), The transition from linear to diffuse plate boundary in the Azores-Gibraltar region: Results from a thin-sheet model, *Earth Planet. Sci. Lett.*, 192, 175–189.

Kaz'min, V. G., A. N. Marova, G. N. Alekhina, and N. F. Tikhonova (1990), Neogene-quaternary deformation of the oceanic lithosphere in the vicinity of Gorringe Bank, Atlantic Ocean, *Int. Geol. Rev.*, 32, 1241–1249.

King, S. D., and D. L. Anderson (1998), Edge-driven convection, *Earth Planet. Sci. Lett.*, 160, 289–296.

Klitgord, K. D., and H. Schouten (1986), Plate kinematics of the central Atlantic, in *The Geology of North America*, vol. M, *The Western North Atlantic Region*, edited by P. R. Vogt and B. E. Tucholke, pp. 351–377, Geol. Soc. of Am., Boulder, Colo.

Kogiso, T., M. M. Hirschmann, and M. Pertermann (2004), High-pressure partial melting of mafic lithologies in the mantle, *J. Petrol.*, 45, 2407–2422.

Laughton, A. S., M. N. Hill, and T. D. Allen (1960), Geophysical investigations of a seamount 150 miles north of Madeira, *Deep Sea Res.*, 7, 117–141.

Le, J., and N. Shackleton (1992), Carbonate dissolution fluctuations in the western equatorial Pacific during the late Quaternary, *Paleoceanography*, 7, 21–42.

Le Bas, M. J., R. W. Le Maitre, A. Streckeisen, and B. Zanettin (1986), A chemical classification of volcanic rocks based on the total alkali-silica diagram, *J. Petrol.*, 27, 745–750.

Lee, D. C., and A. N. Halliday (1995), Precise determination of the isotope compositions and atomic weights of molybdenum, tellurium, tin and tungsten using ICO magnetic sector multiple collector mass spectrometry, *Int. J. Mass Spectrom. Ion Processes*, 146/147, 35–46.

Le Fèvre, B., and C. Pin (2001), An extraction chromatography method for Hf separation prior to isotopic analysis using multiple collection ICP-mass spectrometry, *Anal. Chem.*, 73, 2453–2460.

Maréchal, C. N., P. Télouk, and F. Albarède (1999), Precise analysis of copper and zinc isotopic compositions by plasma-source mass spectrometry, *Chem. Geol.*, 156, 251–273.

Mata, J., R. Kerrich, N. D. MacRae, and T. -W. Wu (1998), Elemental and isotopic (Sr, Nd, and Pb) characteristics for a composite HIMU-EM I plume fertilizing lithosphere, *Can. J., Earth Sci.*, 35, 980–997.

McCulloch, M. T., K. J. R. Rosman, and J. R. De Laeter (1977), The isotopic and elemental abundance of ytterbium in meteorites and terrestrial samples, *Geochim. Cosmochim. Acta*, 41, 1703–1707.

Morgan, W. J. (1983), Hotspot tracks and the early rifting of the Atlantic, *Tectonophysics*, 94, 123–139.

Nederbragt, A. J. (1991), Late Cretaceous biostratigraphy and development of Heterohelicidae (planktic foraminifera), *Micropaleontology*, 37(4), 329–372.

Parés, J. M., and T. C. Moore (2005), New evidence for the Hawaiian hotspot plume motion since the Eocene, *Earth Planet. Sci. Lett.*, 237, 951–959.

Patchett, P. J., and M. Tatsumoto (1980), Hafnium isotope variations in oceanic basalts, *Geophys. Res. Lett.*, 7, 1077–1080.

Peirce, C., and P. J. Barton (1991), Crustal structure of the Madeira-Tore Rise, eastern North Atlantic-results of a DOBS wide-angle and normal incidence seismic experiment in the Josephine Seamount region, *Geophys. J. Int.*, 106, 357–378.

Pe-Piper, G., A. de Jonge, D. J. W. Piper, and L. F. Jansa (2003), Morphology, petrography, age and origin of Fogo Seamount chain, offshore eastern Canada, *Geophys. Res. Abstr.*, 5, 02020.

Premoli Silva, I., and W. V. Sliter (1999), Cretaceous paleoceanography: Evidence from planktonic foraminiferal evolution, in *Evolution of the Cretaceous Ocean-Climate System*, edited by E. Barrera and C. C. Johnson, *Spec. Pap. Geol. Soc. Am.*, 332, 301–328.

Robaszynski, F., and M. Caron (1995), Foraminifères planctoniques du Crétacé; commentaire de la zonation Europe-Mediterranée, *Bull. Soc. Géol. Fr.*, 166(6), 81–692.

Roeser, H. A., C. Steiner, B. Schreckenberger, and M. Block (2002), Structural development of the Jurassic Magnetic Quiet Zone off Morocco and

identification of Middle Jurassic magnetic lineations, *J. Geophys. Res.*, *107*(B10), 2207, doi:10.1029/2000JB000094.

Royden, L. H. (1993), Evolution of retreating subduction boundaries formed during continental collision, *Tectonics*, *12*(13), 629–638.

Russel, W. A., D. A. Papanastassiou, and T. A. Tombrello (1978), Ca isotope fractionation on the Earth and other solar system materials, *Geochim. Cosmochim. Acta*, *42*, 1075–1090.

Schärer, U., J. Girardeau, G. Cornen, and G. Boillot (2000), 138-121 Ma asthenospheric magmatism prior to continental break-up in the North Atlantic and geodynamic implications, *Earth Planet. Sci. Lett.*, *181*, 555–572.

Schwarz, S., A. Klügel, P. v. d. Bogaard, and J. Geldmacher (2005), Internal structure of a volcanic rift system in the eastern North Atlantic: The desert as rift zone, Madeira archipelago, *J. Volcanol. Geotherm. Res.*, *141*, 123–155.

Sleep, N. H. (1990), Monteregian hotspot track: A long-lived mantle plume, *J. Geophys. Res.*, *95*, 21,983–21,990.

Sleep, N. H. (2002), Ridge-crossing mantle plumes and gaps in tracks, *Geochem. Geophys. Geosyst.*, *3*(12), 8505, doi:10.1029/2001GC000290.

Smith, W. H. F., and D. T. Sandwell (1997), Global seafloor topography from satellite altimetry and ship depth soundings, *Science*, *277*, 1956–1962.

Srivastava, S. P., J.-C. Sibuet, S. Cande, W. R. Roest, and I. D. Reid (2000), Magnetic evidence for slow seafloor spreading during the formation of the Newfoundland and Iberian margins, *Earth Planet. Sci. Lett.*, *182*, 61–76.

Steinberger, B. (2002), Motion of the Easter hot spot relative to Hawaii and Louisville hot spots, *Geochem. Geophys. Geosyst.*, *3*(11), 8503, doi:10.1029/2002GC000334.

Steinberger, B., and R. J. O'Connell (1998), Advection of plumes in mantle flow: Implications for hot spot motion, mantle viscosity and plume distribution, *Geophys. J. Int.*, *132*, 412–434.

Sullivan, K. D., and C. E. Keen (1977), Newfoundland seamounts: Petrology and geochemistry, *Geol. Assoc. Can. Spec. Pap.*, *16*, 461–476.

Sun, S. S., and W. F. McDonough (1989), Chemical and isotopic systematics of oceanic basalts: Implications for mantle composition and processes, in *Magmatism in the Ocean Basins*, *Spec. Publ. 42*, edited by A. D. Saunders and M. J. Norrey, pp. 313–345, Geol. Soc. of Am., Boulder, Colo.

Taras, B. D., and S. R. Hart (1987), Geochemical evolution of the New England Seamount chain: Isotopic and trace element constraints, *Chem. Geol.*, *64*, 35–54.

Tarduno, J. A., et al. (2003), The Emperor Seamounts: Southward motion of the Hawaiian hotspot plume in the Earth mantle, *Science*, *301*, 1064–1069.

Thirlwall, M. F., and R. Anczkiewicz (2004), Multidynamic isotope ratio analysis using MC-ICP-MS and the causes of secular drift in Hf, Nd and Pb isotope ratios, *Int. J. Mass Spectrom.*, *235*, 59–81.

Todt, W., R. A. Cliff, A. Hanser, and A. W. Hofmann (1996), Evaluation of a ^{202}Pb-^{205}Pb double spike for high precision lead isotope analyses, in *Earth Processes: Reading the Isotopic Code*, *Geophys. Monogr. Ser.*, vol. 95, edited by A. Basu and S. Hart, pp. 429–437, AGU, Washington, D. C.

Tucholke, B. E., and W. J. Ludwig (1982), Structure and origin of the J-Anomaly Ridge, western North Atlantic Ocean, *J. Geophys. Res.*, *87*, 9389–9407.

Tucholke, B. E., and N. C. Smoot (1990), Evidence for age and evolution of Corner Seamounts and Great Meteor Seamount chain from multibeam bathymetry, *J. Geophys. Res.*, *95*, 17,555–17,569.

Tucholke, B. E., and P. R. Vogt (1979), Western North Atlantic: Sedimentary evolution and aspects of tectonic history, *Initial Rep. Deep Sea Drill. Proj.*, *43*, 791–825.

Tucholke, B. E., et al. (1979), Site 384. The Cretaceous/Tertiary boundary, Aptian reefs, and the J-Anomaly Ridge, *Initial Rep. Deep Sea Drill. Proj.*, *43*, 107–165.

Ulfbeck, D., J. Baker, T. Waight, and E. Krogstad (2003), Rapid sample digestion by fusion and chemical separation of Hf for isotopic analysis by MC-ICPMS, *Talanta*, *59*, 365–373.

Vance, D., and M. Thirlwall (2002), An assessment of mass discrimination in MC-ICPMS using Nd isotopes, *Chem. Geol.*, *185*, 227–240.

Weaver, B. L. (1991), The origin of ocean island basalt end-member compositions: Trace element and isotopic constraints, *Earth Planet. Sci. Lett.*, *104*, 381–397.

Wendt, I., et al. (1976), K-Ar age of basalts from Great Meteor and Josephine seamounts (eastern North Atlantic), *Deep Sea Res.*, *23*(9), 849–862.

Weyer, S., C. Münker, M. Rehkämper, and K. Mezger (2002), Determination of ultra-low Nb, Ta, Zr and Hf concentrations and the chondritic Zr/Hf and Nb/Ta ratios by isotope dilution analyses with multiple collector ICP-MS, *Chem. Geol.*, *187*, 295–313.

Wieser, M. E., and J. B. Schwieters (2005), The development of multiple collector mass spectrometry for isotope ratio measurements, *Int. J. Mass. Spectrom.*, *242*, 97–115.

Wombacher, F., and M. Rehkämper (2003), Investigation of the mass discrimination of multiple collector ICP-MS using neodymium isotopes and the generalised power law, *J. Anal. At. Spectrom.*, *18*, 1371–1375.

————————

B. Berning, Institute of Geology and Paleontology, Universität Graz, Heinrichstr. 26, 8010 Graz, Austria.

P. v. d. Bogaard, J. Geldmacher, and K. Hoernle, Leibniz Institute of Marine Sciences, IFM-GEOMAR, Wischhofstr. 1-3, D-24148 Kiel, Germany. (jgeldmacher@ifm-geomar.de)

A. Klügel, Department of Geosciences, Universität Bremen, Postfach 33 04 40, D-28334 Bremen, Germany.

F. Wombacher, FR Geochemistry, Freie Universität Berlin, Malteserstr. 74-100, D-12249 Berlin, Germany.